

Equilibrium sequences of differentially rotating stars with post-merger-like rotational profiles

Panagiotis Iosif¹★ and Nikolaos Stergioulas¹

¹*Department of Physics, Aristotle University of Thessaloniki, Thessaloniki 54124, Greece*

Accepted XXX. Received YYY; in original form ZZZ

ABSTRACT

We present equilibrium sequences of rotating relativistic stars, constructed with a new rotation law that was proposed by Uryu et al. (2017). We choose rotational parameters motivated by simulations of binary neutron star merger remnants, but otherwise adopt a cold, relativistic $N = 1$ polytropic EOS, in order to perform a detailed comparison to published equilibrium sequences that used the Komatsu, Eriguchi and Hachisu (1989) rotation law. We find a small influence of the choice of rotation law on the mass of the equilibrium models and a somewhat larger influence on their radius. The versatility of the new rotation law allows us to construct models that have a similar rotational profile and axis ratio as observed for merger remnants, while at the same time being quasi-spherical. More specifically, we construct equilibrium sequence variations with different degrees of differential rotation and identify type A and type C solutions, similar to the corresponding types in the classification of Ansorg, Gondek-Rosińska and Villain (2009). While our models are highly accurate solutions of the fully general relativistic structure equations, we demonstrate that for models relevant to merger remnants the IWM-CFC approximation still maintains an acceptable accuracy.

Key words: stars: neutron – stars: rotation – methods: numerical – relativistic processes – stars: kinematics and dynamics – equation of state

1 INTRODUCTION

Gravitational waves detected from the GW170817 neutron star merger event (Abbott et al. 2017a) and complementary information from its electromagnetic counterpart (Abbott et al. 2017b; Goldstein et al. 2017) were pivotal in confirming the broad picture describing the possible outcomes of a binary neutron star (BNS) merger. The behaviour of the binary is closely tied to the equation of state (EOS) and the total mass $M = m_1 + m_2$ of the system, where m_1 and m_2 are the binary’s components masses. Depending on where exactly M stands compared to three distinct fundamental mass values, will determine the evolution of the BNS (see Shibata & Hotokezaka (2019); Bernuzzi (2020); Friedman & Stergioulas (2020) for recent reviews).

A first checkpoint is the comparison of the total mass M to the M_{thres} value, which is the threshold mass above which the merger remnant immediately collapses to a black hole. If $M < M_{\text{thres}}$, the merger results in a hot, massive and differentially rotating, compact object with a substantial material disk around it. In this scenario, another mass comes into play, namely the maximum mass of a cold, uniformly rotating neutron star, $M_{\text{max,rot}}$. If $M > M_{\text{max,rot}}$, the remnant can survive several tens of milliseconds (ms) due to the support of differential rotation and thermal pressure. Collapse to a black hole is inevitable though. Dissipative effects (e.g. effective viscosity due to the development of the magneto-rotational instability, see Shibata & Hotokezaka (2019); Cioffi (2020) for recent reviews and also Radice (2020)), allow uniform rotation to set in, leading to a delayed

collapse to a black hole. Other mechanisms that enforce uniform rotation in differentially rotating remnants are magnetic braking and shear viscosity. Finally, if $M < M_{\text{max,rot}}$, another mass comparison is in order, this time with M_{max} , which is the maximum mass of a cold, nonrotating star. After differential rotation is effectively damped, the configuration settles down to rigid rotation. However, since the magnetic field generated during the merger will spin the star down, when the remnant’s rotational kinetic energy is dissipated the configuration will eventually collapse to a black hole, unless $M < M_{\text{max}}$, in which case a cold, nonrotating neutron star will be the final outcome.

After the initial period of the remnant’s formation (i.e. the first few ms), a phase that is highly nonlinear, it is possible to regard the system as a quasi-stationary, slowly drifting equilibrium state with the addition of oscillations, that are close to the linear normal modes (quasi-linear combination tones also appear) and of a spiral deformation (Stergioulas et al. 2011; Bauswein & Stergioulas 2015; Bauswein et al. 2016; Bauswein & Stergioulas 2019). Ignoring some aspects of the state of the remnant (non-axisymmetric deformations, oscillations, time-dependence, thermal structure), can lead to simplified models of its structure, with varying degree of accuracy.

In this context and depending on the two initial neutron star masses and EOS describing stellar matter, the remnant can be approximated during the various phases of its lifetime, as either a hypermassive neutron star (HMNS), or a supramassive neutron star (SMNS). In connection to the three critical masses mentioned above, a uniformly rotating star is called supramassive when its rest mass exceeds the maximum rest mass M_{max} of a nonrotating star constructed with the same EOS (Cook et al. 1992). If it is uniformly rotating, its mass is

★ E-mail: piosif@auth.gr

limited by the mass-shedding limit for uniform rotation (also called Kepler limit). In the case of a HMNS the star can only be differentially rotating. The mass of a HMNS falls in the range $M_{\text{max,rot}} < M < M_{\text{thres}}$, i.e. it is below the prompt collapse threshold and above the maximum limit for rigid rotation (Baumgarte et al. 2000).

Numerical simulations have been the primary tool to study compact binary coalescences and have supplied a wealth of information during the last two decades. Long-lived merger remnants (i.e. with a lifetime greater than 10ms) have been reported by e.g. Hotokezaka et al. (2011); Sekiguchi et al. (2011); Bauswein & Janka (2012); Bauswein et al. (2012); Hotokezaka et al. (2013); Bernuzzi et al. (2014); Dietrich et al. (2015); De Pietri et al. (2016); Radice et al. (2018), whereas the remnant's rotational profile was studied extensively in a variety of setups (Kastaun & Galeazzi 2015; Bauswein & Stergioulas 2015; Kastaun et al. 2016; Endrizzi et al. 2016; Kastaun et al. 2017; Cioffi et al. 2017; Hanauske et al. 2017; Endrizzi et al. 2018; Kiuchi et al. 2018; Cioffi et al. 2019; East et al. 2019; De Pietri et al. 2020). A common finding of the aforementioned works is that the remnant's rotation profile exhibits a maximum away from the center, that shows only a modest dependence on the exact EOS employed. This is in sharp disagreement with the differential rotation law by Komatsu et al. (1989), hereafter KEH, which is widely used in the literature in the context of differentially rotating neutron stars and is characterised by a monotonic decline of the angular velocity Ω (for an extensive exploration of different types of equilibrium models that are possible with the KEH rotation law, see Ansorg et al. 2009; Espino & Paschalidis 2019; Espino et al. 2019). Rotational profiles for BNS merger remnants in eccentric mergers have been reported in Paschalidis et al. (2015); East et al. (2016).

The need of a more realistic rotation law to construct equilibrium models of differentially rotating BNS remnants was first tackled by Galeazzi et al. (2012), who introduced a new parametrized functional form of the rotational profile that enabled the reproduction of different power laws in the outer envelope of the angular velocity distribution. A further step was taken by Uryū et al. (2016), who suggested a simple generalized differential rotation law, which could cover various cases using two parameters. Building up on this work, a subsequent study by Uryū et al. (2017) made a more systematic suggestion of new formulations for modelling differential rotation of compact stars, among which were a 3-parameter and a 4-parameter rotation law. Uryū et al. presented selected solutions of differentially rotating, stationary, and axisymmetric compact stars in equilibrium, as examples of their proposed rotation laws. Other works that explored departure from the common Komatsu et al. (1989) rotation law were Bauswein & Stergioulas (2017); Bozzola et al. (2018), where a 3-parameter piecewise extension of the Komatsu et al. law was used to distinguish two different regions inside the star. In this way, the envelope was allowed to rotate more slowly, so that stars could reach higher masses (typical for remnants) without encountering mass-shedding.

For the case of disks around black holes, recently, a new 4-parameter family of rotation laws has also been considered, describing single rotating toroids and toroids rotating around black holes (Mach & Malec 2015). Karkowski et al. (2018) have studied an extension of the Mach & Malec law, proposing a general relativistic Keplerian rotation law for self-gravitating disks around spinning black holes. Furthermore, a generalisation of the above laws to non-Keplerian rotation has been suggested by Kulczycki & Malec (2020).

After the work of Uryū et al. (2017), several authors started investigating the newly suggested laws for modelling realistic rotational profiles of differentially rotating, relativistic stars. Zhou et al. (2019) employed the 4-parameter nonmonotonic rotation law of Uryū et al.

to construct differentially rotating strange star models investigating their maximum mass, toroidal solutions and the relationship between the threshold mass for prompt collapse to a black hole and angular momentum. Passamonti & Andersson (2020) studied the 3-parameter rotation law of Uryū et al. and its impact on the low $T/|W|$ instability (Watts et al. 2005), using time evolutions of the linearised dynamical equations in Newtonian gravity, to study nonaxisymmetric oscillations and identify the unstable modes. Xie et al. (2020) continued the study of Passamonti & Andersson with a fully relativistic initial survey of the nonlinear effects associated with unstable modes for different rotation laws, employing the 3-parameter rotation law of Uryū et al. as well.

In light of recent works, the motivation for this study is to explore the new 4-parameter differential rotation by Uryū et al. as a more realistic and versatile option for modelling compact BNS merger remnants. Our aim is to present a first systematic study of equilibrium models constructed with the new rotation law and investigate their properties.

The structure of the paper is as follows: in Section 2 we present the general framework of this study. The basic equations are laid out in Section 2.1, their modifications for the differential rotation law under examination are described in Section 2.2 and a convergence study is presented in Section 2.3. We define the equilibrium sequences that we construct in Section 3.1, compare to the corresponding KEH sequences in Section 3.2. In Section 3.3 we focus on the effect of different values for the rotation law's parameters, while in Section 3.4 we identify different types of solutions corresponding to the different rotation law parameters' values employed. Finally, in Section 4 we present a summary of our main results and some conclusions.

Throughout the text we employ dimensionless units for all physical quantities by setting $c = G = M_{\odot} = 1$.

2 METHOD

2.1 Framework and basic equations

For this work, we construct stationary, axisymmetric equilibrium stellar models, with matter described as a perfect fluid. We refer to Friedman & Stergioulas (2013); Paschalidis & Stergioulas (2017), for a more detailed exposition.

The line element for a stationary, axisymmetric star in full general relativity (GR) can be written in the form

$$ds^2 = -e^{\gamma+\rho} dt^2 + e^{\gamma-\rho} r^2 \sin^2 \theta (d\phi - \omega dt)^2 + e^{2\mu} (dr^2 + r^2 d\theta^2), \quad (1)$$

where γ , ρ , ω and μ are metric functions depending only on the coordinates r and θ . We assume the usual polytropic EOS

$$p = K\rho^{1+\frac{1}{N}}, \quad (2)$$

for which the first law of thermodynamics gives

$$\epsilon = \rho + Np, \quad (3)$$

where p is the pressure, ρ is the rest mass density, ϵ is the energy density, K is the polytropic constant and N is the polytropic index. Note that one should not confuse the metric function ρ with the rest mass density, since the quantity meant by the symbol " ρ " should be evident from the relative context.

In order to create our equilibrium models we use the `rns` code (Stergioulas & Friedman 1995). The code is based on the KEH scheme (Komatsu et al. 1989) and includes modifications suggested by Cook et al. (1992).

In all KEH-type codes, starting from an initial guess for the metric

potentials γ , ρ , ω , μ , the energy density ϵ and the angular velocity Ω , one uses the first integral of the hydrostationary equilibrium and the specified EOS to obtain an updated matter distribution. Subsequently, the γ , ρ , ω and μ distributions are updated and the steps are resumed until convergence to a solution is achieved. One of the basic steps of the scheme is to find a new angular velocity distribution in each iteration. Initially, we need a new value for the angular velocity at the equator, Ω_e , then for the angular velocity at the rotation axis, Ω_c and finally a new Ω distribution everywhere inside the star.

In order to tackle these requirements, we need to start with the equation of motion. The projection of the conservation of the stress-energy tensor orthogonal to the 4-velocity u^α is

$$q^\alpha_\gamma \nabla_\beta T^{\beta\gamma} = 0, \quad (4)$$

where

$$q^{\alpha\beta} = g^{\alpha\beta} + u^\alpha u^\beta \quad (5)$$

is the projection operator orthogonal to u^α , with $g_{\alpha\beta}$ being the spacetime metric and

$$T^{\alpha\beta} = \epsilon u^\alpha u^\beta + p q^{\alpha\beta} \quad (6)$$

the stress-energy tensor. The projection (4) gives rise to the relativistic Euler equation, which for the case of a stationary, axisymmetric star has the form

$$\begin{aligned} \frac{\nabla_\alpha p}{(\epsilon + p)} &= -u^\beta \nabla_\beta u_\alpha \\ &= \nabla_\alpha \ln u^t - u^t u_\phi \nabla_\alpha \Omega. \end{aligned} \quad (7)$$

For barotropes, since $\epsilon = \epsilon(p)$, we can define a function

$$H(p) := \int_0^p \frac{dp'}{\epsilon(p') + p'}, \quad (8)$$

that satisfies

$$\nabla H = \nabla \ln h - \frac{T}{h} \nabla s, \quad (9)$$

where $h = (\epsilon + p)/\rho$ is the specific enthalpy (i.e. the enthalpy per unit rest mass), T is the temperature and s is the specific entropy (i.e. the entropy per unit rest mass). Taking into account (8), the Euler equation (7) is written as

$$\nabla(H - \ln u^t) = -F \nabla \Omega, \quad (10)$$

where $F = u^t u_\phi$, i.e. F denotes the gravitationally redshifted angular momentum per unit rest mass and enthalpy. If we consider stars with a homogeneous entropy distribution, then from (9) it follows that, up to a constant, $H = \ln h$ and the hydrostationary equilibrium equation is written as

$$\nabla \left(\ln \frac{h}{u^t} \right) = -F \nabla \Omega. \quad (11)$$

In the case of differential rotation, $F = F(\Omega)$ and Equation (10) gives

$$H - \ln u^t + \int_{\Omega_{\text{pole}}}^{\Omega} F(\Omega') d\Omega' = \text{constant}, \quad (12)$$

where the lower Ω integration limit is chosen as the value of Ω at the pole, where H and the 3-velocity v measured in the frame of a zero angular momentum observer (ZAMO) vanish.

In order to obtain a new value for the angular velocity at the equator Ω_e , we need to equate the first integral of the hydrostationary equilibrium (12) at the equator to its value at the pole and solve the resulting expression numerically. This step involves making a

choice for the differential rotation law describing the models that we construct, namely the function $F(\Omega)$.

Until recently, the majority of works that tackled equilibrium modelling and differential rotation followed KEH in adopting a simple, computationally convenient, differential rotation law of the form,

$$F(\Omega) = A^2(\Omega_c - \Omega), \quad (13)$$

where A is a positive constant that determines the length scale over which the angular velocity Ω changes within the star and Ω_c is the angular velocity at the center of the configuration. Rotation law (13) is reduced to uniform rotation for $A \rightarrow \infty$ and to the j -constant law for $A \rightarrow 0$. Here, $j = hu_\phi$ is the specific angular momentum, i.e. the angular momentum per unit baryon mass, consistent with the integral expression of the total angular momentum $J = \int j dM_0$. We note that along an axisymmetric flow the specific angular momentum j is conserved, i.e. its Lie derivative vanishes, $\mathcal{L}_u(hu_\phi) = 0$.

For this study, the version of the `rns` code used in Stergioulas et al. (2004) was expanded in order to implement the 4-parameter rotation law introduced in Uryū et al. (2017)

$$\Omega = \Omega_c \frac{1 + \left(\frac{F}{B^2 \Omega_c} \right)^p}{1 + \left(\frac{F}{A^2 \Omega_c} \right)^{q+p}}, \quad (14)$$

(hereafter Uryū+ law), where p controls the growth of the rotation curve near the rotation axis and q controls the asymptotic behavior of $\Omega(r)$ (setting $q = 3$ results in recovering the Keplerian rotation law in the Newtonian limit). In this work, we choose the values $\{p, q\} = \{1, 3\}$, for which the integral in (12) can be calculated analytically.

Here, we should point out that in the case of the transient compact remnant formed after a BNS merger, the numerically extracted $\Omega(r)$ profile in the equatorial plane, implies that $F(\Omega)$ is not a one-to-one function. In order to overcome this problem, we need to consider $\Omega = \Omega(F)$, instead of $F = F(\Omega)$ (Uryū et al. 2017). This means that the integral in Equation (12) must be rearranged as

$$\int F d\Omega = \int F \frac{d\Omega}{dF} dF. \quad (15)$$

As far as the parameters A , B in the rotation law (14) are concerned, we follow Uryū et al. (2017); Zhou et al. (2019) and instead of explicitly exploring different values for A and B , we opt to fix the ratios of the maximum angular velocity over the angular velocity at the center of the configuration, $\Omega_{\text{max}}/\Omega_c$, and of the angular velocity at the equator over the angular velocity at the center, Ω_e/Ω_c , to certain selected values. We determine the value of the parameters A and B by solving for them in each iteration. Furthermore, we implement the aforementioned Ω ratios as extra input parameters in the `rns` code, so that we can investigate their influence on representative equilibrium models of each sequence (Table 3). We denote these parameters as

$$\lambda_1 = \frac{\Omega_{\text{max}}}{\Omega_c}, \quad (16)$$

$$\lambda_2 = \frac{\Omega_e}{\Omega_c}. \quad (17)$$

We note that as reference values for the ratios $\{\lambda_1, \lambda_2\}$ we adopt the choice $\{2.0, 0.5\}$ as in Uryū et al. (2017). Equilibrium models reported in Tables 1, 2 and B1 are computed using these reference values, whereas later we also explore other values of $\{\lambda_1, \lambda_2\}$ both for selected equilibrium models (Table 3) and full sequences (Table 4).

2.2 Implementation of the Uryu+ rotation law

Having specified the differential rotation law we are interested in, we can return to the first integral of the hydrostationary equilibrium (12) and apply it at the pole and equator, in order to compute a new value for Ω_e . We substitute the following expressions for the 4-velocity component u^t and the 3-velocity v

$$u^t = \frac{e^{-(\gamma+\rho)/2}}{\sqrt{1-v^2}}, \quad (18)$$

and

$$v = (\Omega - \omega) r \sin \theta e^{-\rho}, \quad (19)$$

in (12) to obtain:

$$\frac{1}{2} (\gamma_e + \rho_e - \gamma_p - \rho_p) + \frac{1}{2} \ln \left[1 - (\Omega_e - \omega_e)^2 r_e^2 e^{-2\rho_e} \right] + \int_0^{F_e} F \frac{d\Omega}{dF} dF = 0. \quad (20)$$

In the above equation, we need to differentiate the $\Omega(F)$ law, calculating the law's parameters in the process. We solve the system of equations for ratios λ_1 and λ_2 to determine expressions for parameters A and B

$$\lambda_1 = \frac{1 + \left(\frac{F_{\max}}{B^2 \Omega_c} \right)^p}{1 + \left(\frac{F_{\max}}{A^2 \Omega_c} \right)^{q+p}}, \quad (21)$$

$$\lambda_2 = \frac{1 + \left(\frac{F_e}{B^2 \Omega_c} \right)^p}{1 + \left(\frac{F_e}{A^2 \Omega_c} \right)^{q+p}}, \quad (22)$$

and for the general $\{p, q\}$ case we find

$$A^2 = \left[\frac{(F_e F_{\max})^p}{\Omega_c^{p+q}} \frac{(\lambda_2 F_e^q - \lambda_1 F_{\max}^q)}{[(\lambda_1 - 1) F_e^p - (\lambda_2 - 1) F_{\max}^p]} \right]^{\frac{1}{p+q}}, \quad (23)$$

and

$$B^2 = \frac{F_e F_{\max}}{\Omega_c} \left[\frac{(\lambda_2 F_e^q - \lambda_1 F_{\max}^q)}{[(\lambda_2 (\lambda_1 - 1) F_e^{p+q} - \lambda_1 (\lambda_2 - 1) F_{\max}^{p+q})]} \right]^{1/p}. \quad (24)$$

Assuming that we need the above expressions to be defined in the real numbers domain, a relevant constraint must be fulfilled, due to the numerator of both fractions in (23) and (24), namely

$$F_e > \left(\frac{\lambda_1}{\lambda_2} \right)^{1/q} F_{\max}. \quad (25)$$

Having secured analytic expressions for the parameters A and B, we differentiate $\Omega(F)$ from expression (14), calculate the integral (15), substitute into (20) and use logarithmic and trigonometric identities to get the expression (for the case that $\{p, q\} = \{1, 3\}$)

$$\begin{aligned} & (\gamma_e + \rho_e - \gamma_p - \rho_p) + \ln \left[1 - (\Omega_e - \omega_e)^2 r_e^2 e^{-2\rho_e} \right] = -2F_e \Omega_e \\ & + \frac{A^2 \Omega_c^2}{2} \left\{ 2 \frac{A^2}{B^2} \arctan \left(\frac{F_e^2}{A^4 \Omega_c^2} \right) - \sqrt{2} \left[\arctan \left(1 - \frac{F_e \sqrt{2}}{A^2 \Omega_c} \right) \right. \right. \\ & \left. \left. - \arctan \left(1 + \frac{F_e \sqrt{2}}{A^2 \Omega_c} \right) \right] + \sqrt{2} \tanh^{-1} \left(\frac{A^2 \Omega_c F_e \sqrt{2}}{F_e^2 + A^4 \Omega_c^2} \right) \right\}. \quad (26) \end{aligned}$$

The above equation needs to be solved numerically, in order to obtain an updated value for Ω_e . Equation (26) involves occurrences of F_e and Ω_c , which need to be expressed in terms of Ω_e , so that a numerical solution can properly take place. The former can be eliminated using the expression $F = u^t u_\phi$,

$$F = \frac{v^2}{(1-v^2)(\Omega - \omega)} = \frac{(\Omega - \omega) r^2 \sin^2 \theta e^{-2\rho}}{\left[1 - (\Omega - \omega)^2 r^2 \sin^2 \theta e^{-2\rho} \right]}, \quad (27)$$

applied at the equator

$$F_e = \frac{(\Omega_e - \omega_e) r_e^2 e^{-2\rho_e}}{\left[1 - (\Omega_e - \omega_e)^2 r_e^2 e^{-2\rho_e} \right]}. \quad (28)$$

The latter can be replaced using the definition of λ_2 (17)

$$\Omega_c = \frac{1}{\lambda_2} \Omega_e, \quad (29)$$

so that in the end, on both hand sides of (26) only the quantity Ω_e is encountered.

For the sake of completeness, we should point out that after obtaining a new value for Ω_e through the solution of (26), a new value for Ω_c can be obtained through (29) and a new distribution of Ω is obtained everywhere inside the star by numerically solving the expression

$$\Omega = \Omega_c \frac{1 + \left(\frac{(\Omega - \omega) r^2 \sin^2 \theta e^{-2\rho}}{B^2 \Omega_c \left[1 - (\Omega - \omega)^2 r^2 \sin^2 \theta e^{-2\rho} \right]} \right)^p}{1 + \left(\frac{(\Omega - \omega) r^2 \sin^2 \theta e^{-2\rho}}{A^2 \Omega_c \left[1 - (\Omega - \omega)^2 r^2 \sin^2 \theta e^{-2\rho} \right]} \right)^{p+q}}, \quad (30)$$

which emerges by combining equations (14) and (27).

With an updated Ω distribution at hand, courtesy of (30), the iterative algorithm moves on to update the matter distribution, a step for which we need a new enthalpy relation compatible with the new Uryu+ rotation law (14). In order to accomplish this, we solve the first integral of the hydrostationary equilibrium and equate its value at an arbitrary point anywhere inside the star to its value at the pole. In the context of the fixed-point iteration in the KEH scheme, the following expression applies generally, regardless of which specific rotation law we choose

$$H = H_{\text{surface}} + \ln \frac{u^t}{u_{\text{pole}}^t} - \int_{\Omega_c}^{\Omega} F(\Omega') d\Omega'. \quad (31)$$

For the case of the Uryu+ law in particular, the integral in (31) is given by the expression (we note that its calculation was already required to obtain Equation (26))

$$\begin{aligned} \int_{\Omega_c}^{\Omega} F(\Omega') d\Omega' &= \int_0^F F' \frac{d\Omega}{dF'} dF' = \\ & F\Omega - \frac{A^2 \Omega_c^2}{4} \left\{ \frac{2A^2}{B^2} \arctan \left(\frac{F^2}{A^4 \Omega_c^2} \right) \right. \\ & \left. - \sqrt{2} \left[\arctan \left(1 - \frac{F\sqrt{2}}{A^2 \Omega_c} \right) - \arctan \left(1 + \frac{F\sqrt{2}}{A^2 \Omega_c} \right) \right] \right. \\ & \left. + \sqrt{2} \tanh^{-1} \left(\frac{A^2 \Omega_c F \sqrt{2}}{F^2 + A^4 \Omega_c^2} \right) \right\}, \quad (32) \end{aligned}$$

where (27) was used.

Here, we should point out that while running the extended rns

Table 1. Convergence study for a rapidly rotating model of high compactness, constructed with the Uryu+ rotation law (14). The model has a central energy density of $\epsilon_c = 3.3 \times 10^{-3}$ and an axis ratio of $r_p/r_e = 0.43$ (this is model C6 calculated with $\{\lambda_1, \lambda_2\} = \{2.0, 0.5\}$ in Section 3 and Table 4). The first column shows the resolution used in the (s, μ) grid of the *rns* code. The remaining columns show the maximum energy density ϵ_{\max} , the gravitational mass M , the rest mass M_0 , the angular momentum J , the ratio of the rotational kinetic energy T over the absolute value of the gravitational binding energy $|W|$, the angular velocity at the rotation axis Ω_c , the maximum value of angular velocity Ω_{\max} , the angular velocity at the equator Ω_e , the angular velocity of a free particle in circular orbit at the equator Ω_K , the circumferential radius R_e , the coordinate radius r_e at the equator and the 3-dimensional general relativistic virial index GRV3. All quantities are reported in dimensionless units $c = G = M_\odot = 1$, in which we choose $K = 100$ for the $N = 1$ polytropic EOS. The last line displays the convergence order, based on the last three resolutions, except for M , M_0 , for which the first three resolutions were used.

resolution SDIV \times MDIV	ϵ_{\max} ($\times 10^{-3}$)	M	M_0	J	$T/ W $ ($\times 10^{-1}$)	Ω_c ($\times 10^{-2}$)	Ω_{\max} ($\times 10^{-2}$)	Ω_e ($\times 10^{-2}$)	Ω_K ($\times 10^{-2}$)	R_e	r_e	GRV3 ($\times 10^{-5}$)
201 \times 101	3.78409	2.27105755	2.477858	3.95626	1.93275	7.22571	14.4641	3.61286	5.98030	8.47078	5.80855	24.3253
401 \times 201	3.78249	2.27111885	2.477878	3.95707	1.93325	7.22415	14.4497	3.61208	5.97857	8.47236	5.81006	8.84179
801 \times 401	3.78169	2.27113957	2.477881	3.95736	1.93348	7.22363	14.4473	3.61181	5.97797	8.47292	5.81060	5.31201
1601 \times 801	3.78156	2.27113961	2.477876	3.95742	1.93353	7.22351	14.4470	3.61175	5.97783	8.47305	5.81073	4.15341
conv. order	2.5	1.7	2.9	2.2	2.1	2.1	2.8	2.1	2.1	2.1	2.0	

code, we chose to keep the central energy density fixed instead of the maximum energy density. This was an experimental choice that after several trials was found to improve model convergence. However, if we want to be thorough in our analysis, we need to obtain a new relation for calculating r_e for the case that we opt to keep the maximum energy density fixed. The derivation is based on calculating the first integral of the hydrostatary equilibrium (12) at the location of the maximum energy density, equating its value there, to its value at the pole and solving for r_e . The analysis is general and in the current framework it holds regardless of which rotation law we choose (in a similar way as in the derivation of the enthalpy relation). The expression we obtain is

$$r_e^2 = \frac{2H_{\max} + \ln(1 - v_{\max}^2) + 2 \int_{\Omega_c}^{\Omega_{\max}} F(\Omega) d\Omega}{\hat{\gamma}_p + \hat{\rho}_p - \hat{\gamma}_{\max} - \hat{\rho}_{\max}}, \quad (33)$$

where all occurrences of the subscript "max" in Equation (33) denote the corresponding quantities at the location where the density has its maximum value (note that, in contrast to the rest of this paper, even Ω_{\max} is to be interpreted in this way in the above equation). Furthermore, in Equation (33) quantities denoted with a "hat" are rescaled with r_e as described in Appendix A. Replacing the integral term in Equation (33) with the corresponding calculation for the specific rotation law under study (e.g. KEH, Uryu+, etc.) yields the relevant relation for each case. For the case of the Uryu+ law, the integral in (33) is calculated at the location of the energy density maximum via (32).

We need to stress that a generalization of the aforementioned procedure to arbitrary $\{p, q\}$ values is not straightforward. In case we want to study a slightly different rotation law, but still described by (14), e.g. $\{p, q\}$ values other than $\{1, 3\}$, things are not so simple as changing the parameters $\{p, q\}$ to our desired values. The obvious reason is that the integral $\int F' \frac{d\Omega}{dF'} dF'$ would have to be recalculated for the new $\{p, q\}$ values and all the relevant equations where it is involved (i.e. expressions for Ω_e , enthalpy and r_e in the case that the maximum energy density is held fixed), would have to be modified.

As a demonstration, attempting to come up with a general expression for the integral $\int F' \frac{d\Omega}{dF'} dF'$ by leaving the differential rotation law (14) in its general form (without using specific values for $\{p, q\}$), leads to occurrences of the incomplete beta function

$$B_z(a, b) = \int_0^z t^{a-1} (1-t)^{b-1} dt. \quad (34)$$

This adds to the complexity of the problem, compared to the simpler

case of setting $\{p, q\} = \{1, 3\}$. Therefore, a thorough investigation of the possible $\{p, q\}$ range, may prove challenging if one additionally considers non-integer $\{p, q\}$ values.

2.3 EOS and convergence study

In the present study, we choose $N = 1$ and $K = 100$, which is a common choice in the literature for testing numerical codes. Note that for the simple polytropic EOS the results can be rescaled to any other choice of K . In practice, we construct a polytropic model with $K = 1$ and then rescale the results to $K = 100$ ($K^{N/2}$ has units of length). The maximum mass nonrotating model has a central energy density $\epsilon_c = 4.122 \times 10^{-3}$, with a gravitational mass of $M \simeq 1.64$ and a rest mass of $M_0 \simeq 1.8$. For the maximum mass uniformly rotating model (i.e. at the mass-shedding limit) the corresponding values are: $\epsilon_c = 3.34 \times 10^{-3}$ with gravitational mass $M \simeq 1.88$ and rest mass $M_0 \simeq 2.07$. We also note that the nonrotating model C0 has a compactness $M/R \sim 0.2$, while nonrotating models A0 and B0 have a (coinciding) compactness of ~ 0.15 .

The *rns* code uses a uniformly-spaced numerical grid with coordinates (s, μ) , where s is a dimensionless, compactified radial coordinate, defined through

$$r = r_e \frac{s}{1-s}, \quad (35)$$

($s = 0$ corresponds to $r = 0$, $s = 1/2$ corresponds to $r = r_e$ and $s = 1$ corresponds to $r = +\infty$) and $\mu = \cos \theta$.

Table 1 shows the results of a convergence study for a rapidly rotating model of high compactness, constructed with the Uryu+ rotation law (14). The upper left panel of Figure 9 shows the rest mass density distribution in the $x - z$ plane, as reference, while in Figure 1 we present the angular velocity profiles $\Omega(F)$ and $\Omega(r)$ at the equatorial plane. The model has a central energy density of $\epsilon_c = 3.3 \times 10^{-3}$ and an axis ratio of $r_p/r_e = 0.43$ (this is model C6 in Section 3). We demonstrate the convergence of the following quantities with increasing resolution: the central energy density ϵ_c , the maximum energy density ϵ_{\max} , the gravitational mass M , the rest mass M_0 , the angular momentum J and the ratio of the rotational kinetic energy T over the absolute value of the gravitational binding energy $|W|$, the angular velocity at the rotation axis Ω_c , the maximum value of angular velocity Ω_{\max} , the angular velocity at the equator Ω_e , the angular velocity of a free particle in circular orbit at the equator Ω_K , the circumferential radius R_e , the coordinate radius r_e at the equator and the 3-dimensional general relativistic virial

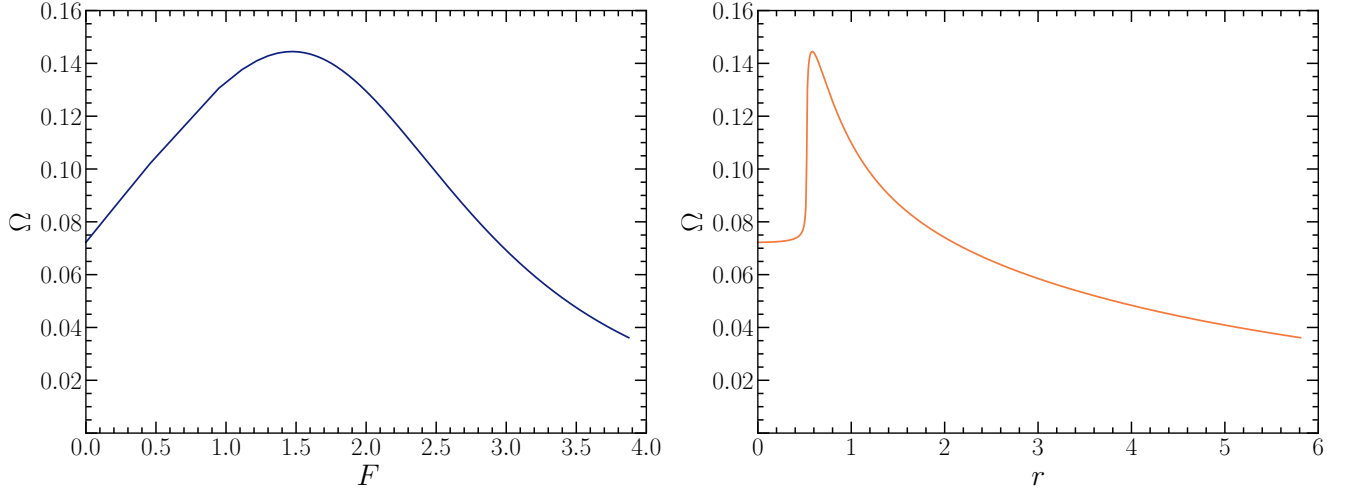


Figure 1. Angular velocity Ω profiles versus the gravitationally redshifted angular momentum per unit rest mass and enthalpy F (left panel) and the coordinate radius r (right panel) in the equatorial plane for model C6 (axis ratio $r_p/r_e = 0.43$), constructed with the Uryu+ rotation law with $\{\lambda_1, \lambda_2\} = \{2.0, 0.5\}$ (see text and Table 4 for details).

index GRV3. The latter has been shown to reflect the accuracy of numerical models of stationary equilibrium configurations (Nozawa et al. 1998).

For the convergence study we use (s, μ) grids of $(\text{SDIV} \times \text{MDIV}) = (201 \times 101)$, (401×201) , (801×401) and (1601×801) . Our results demonstrate 2nd-order convergence, as expected for the overall numerical schemes employed in `rns`. Between the two highest resolutions, the relative difference is less than $\sim 2.6 \times 10^{-5}$ for the integrated quantities $M, M_0, J, T/|W|$ (in particular, for the masses it is less than $\sim 2 \times 10^{-6}$) and less than $\sim 2.3 \times 10^{-5}$ for the local quantities $r_e, R_e, \Omega_c, \Omega_{\max}, \Omega_e, \Omega_K$.

In the remainder of this work, all numerical models will be constructed with a standard resolution of $(\text{SDIV} \times \text{MDIV}) = (801 \times 401)$.

3 SEQUENCES OF EQUILIBRIUM MODELS

3.1 Definition of the equilibrium sequences

For comparison with previous work (Stergioulas et al. 2004; Iosif & Stergioulas 2014), we construct three sequences of equilibrium models using the new differential rotation law (14):

- Sequence A is a constant rest mass sequence with $M_0 = 1.506$.
- Sequence B is a constant central energy density sequence with $\epsilon_c = 1.444 \times 10^{-3}$.
- Sequence C is a constant central energy density sequence with $\epsilon_c = 3.3 \times 10^{-3}$.

We note that the central energy density value of sequence C, which is the most relativistic out of the three sequences, is determined taking into account remarks in Takami et al. (2011) and Giacomazzo et al. (2011) concerning the location of the secular and dynamical instabilities. We note that the faster rotating equilibrium models of sequence C could be both secularly and dynamically unstable. For the KEH rotation law, Weih et al. (2018) showed that the dynamical instability occurs well before the turning points of constant-angular-momentum

sequences¹. See also Friedman & Stergioulas (2013, section 9.2) for a summary on axisymmetric stability and turning points, where the difference between indices Γ (governing the equilibrium EOS) and Γ_1 (governing dynamical oscillations) is highlighted. This means that for realistic (i.e. hot) stars the instability limit will not be the same as in the case of cold stars. In particular, the difference between secular and dynamical instability for hot stars could be larger than the corresponding difference for cold stars.

Tables 2 and 4 list all relevant physical quantities for the three different sequences of equilibrium models. Since we want to compare these models to the corresponding models constructed with the KEH rotation law, we re-calculated sequences A, B (defined in Stergioulas et al. 2004) and C (defined in Iosif & Stergioulas 2014) with the KEH rotation law, using our standard resolution of $(\text{SDIV} \times \text{MDIV}) = (801 \times 401)$. For the KEH sequence A, we kept the same central energy density values and a rest mass of $M_0 = 1.506$ as in Stergioulas et al. (2004), which resulted in slightly different r_p/r_e (due to the different resolution) than those reported in Stergioulas et al. (2004). In addition, for the KEH sequence C, we calculated an additional model with $r_p/r_e = 0.43$, in order to facilitate the comparison with the Uryu+ sequence C for the case of $\{\lambda_1, \lambda_2\} = \{2.0, 0.5\}$ (Figures 5 and 7), since the latter terminates at this axis ratio². The detailed properties of this additional model are displayed in Table C1 in Appendix C. In the Figures 2, 3, 4, 5, 6 and 7 that follow, all models have been constructed assuming $\{\lambda_1, \lambda_2\} = \{2.0, 0.5\}$.

In Figure 2 we plot the gravitational mass M as a function of the central energy density ϵ_c for the three sequences A, B and C. For reference, we show the TOV (nonrotating) sequence as a solid line and the mass-shedding limit for uniform rotation (Kepler limit) as a dashed line. The dotted line represents the axisymmetric stability limit for uniformly rotating models, based on the turning point

¹ The latter are used to locate the secular axisymmetric instability in uniformly rotating stars.

² The termination of sequence C with the Uryu+ rotation law is due to a limitation of the numerical scheme in `rns` - the sequence has not reached the mass-shedding limit, as is evident from the Ω_e vs. Ω_K values of model C6 displayed in Table 4.

Table 2. Physical quantities for sequences A (with constant $M_0 = 1.506$) and B (with constant $\epsilon_c = 1.444 \times 10^{-3}$) calculated using the Uryu+ differential rotation law (14). The different quantities are defined as in Table 1.

Model	r_p/r_e	ϵ_c ($\times 10^{-3}$)	ϵ_{\max} ($\times 10^{-3}$)	M	M_0	J	$T/ W $ ($\times 10^{-1}$)	Ω_c ($\times 10^{-2}$)	Ω_{\max} ($\times 10^{-2}$)	Ω_e ($\times 10^{-2}$)	Ω_K ($\times 10^{-2}$)	R_e	r_e	GRV3 ($\times 10^{-5}$)
A0	1.0	1.444	1.44400	1.40021	1.50624	0.0	0.0	0.0	0.0	0.0	3.98735	9.58537	8.12483	4.94068
A1	0.9350	1.300	1.30000	1.40336	1.50600	0.48978	0.16876	1.13141	2.26283	0.56571	3.76434	9.94733	8.47659	7.78180
A2	0.8834	1.187	1.18700	1.40618	1.50597	0.67872	0.31154	1.46576	2.93153	0.73288	3.60338	10.2712	8.79166	7.34990
A3	0.8312	1.074	1.07400	1.40928	1.50600	0.84681	0.46416	1.69791	3.39582	0.84896	3.43843	10.6376	9.14868	6.99791
A4	0.7783	0.961	0.96100	1.41258	1.50595	1.00873	0.62736	1.86296	3.72593	0.93148	3.26734	11.0556	9.55670	6.71677
A5	0.7243	0.848	0.84800	1.41624	1.50599	1.17284	0.80274	1.97572	3.95145	0.98786	3.08876	11.5380	10.0283	6.47831
A6	0.6689	0.735	0.73500	1.42027	1.50605	1.34476	0.99147	2.04215	4.08430	1.02107	2.90170	12.1014	10.5798	6.30968
A7	0.6117	0.622	0.62200	1.42456	1.50595	1.52957	1.19443	2.06431	4.12863	1.03216	2.70530	12.7680	11.2335	6.16661
A8	0.5519	0.509	0.50900	1.42932	1.50586	1.73385	1.41258	2.04253	4.08507	1.02127	2.49909	13.5694	12.0206	6.05597
A9	0.4882	0.396	0.40086	1.43493	1.50612	1.96591	1.64514	1.97549	3.95098	0.98775	2.28329	14.5499	12.9843	6.03066
A10	0.4183	0.283	0.32884	1.44091	1.50615	2.23263	1.88559	1.86009	3.72018	0.93005	2.05902	15.7684	14.1836	6.17384
A11	0.3356	0.170	0.26606	1.44762	1.50639	2.54338	2.11646	1.69452	3.38903	0.84726	1.82984	17.3064	15.6984	6.57445
A12	0.2798	0.110	0.23676	1.45080	1.50595	2.72584	2.22139	1.58573	3.17146	0.79287	1.70767	18.2887	16.6668	6.72845
B0	1.0	1.444	1.44400	1.40021	1.50624	0.0	0.0	0.0	0.0	0.0	3.98735	9.58537	8.12483	4.94068
B1	0.950	1.444	1.44400	1.43873	1.54893	0.44293	0.12874	1.04200	2.08400	0.52100	3.94463	9.71434	8.20529	7.95499
B2	0.900	1.444	1.44400	1.48252	1.59755	0.67619	0.26495	1.49286	2.98572	0.74643	3.92705	9.85083	8.28676	7.58352
B3	0.849	1.444	1.44400	1.53373	1.65451	0.90387	0.41202	1.86097	3.72193	0.93048	3.91534	9.99772	8.36948	7.21883
B4	0.800	1.444	1.44400	1.59038	1.71769	1.13525	0.56153	2.17462	4.34924	1.08731	3.90946	10.1454	8.44627	6.90944
B5	0.750	1.444	1.44400	1.65729	1.79252	1.39794	0.72279	2.47431	4.94862	1.23716	3.90997	10.3013	8.51829	6.63163
B6	0.700	1.444	1.44400	1.73532	1.88009	1.70054	0.89312	2.76602	5.53204	1.38301	3.91929	10.4592	8.57816	6.38871
B7	0.650	1.444	1.44400	1.82678	1.98317	2.05786	1.07256	3.06059	6.12118	1.53030	3.94107	10.6134	8.61690	6.18202
B8	0.600	1.444	1.44400	1.93428	2.10493	2.48740	1.26069	3.37014	6.74029	1.68507	3.98100	10.7539	8.62050	5.99032
B9	0.550	1.444	1.44400	2.06020	2.24840	3.00859	1.45629	3.71100	7.42200	1.85550	4.04785	10.8636	8.56761	5.81028
B10	0.500	1.444	1.48092	2.20535	2.41490	3.63795	1.65695	4.10748	8.21495	2.05374	4.15491	10.9145	8.42730	5.64007
B11	0.450	1.444	1.62233	2.36580	2.60021	4.37467	1.85864	4.59661	9.19322	2.29830	4.32118	10.8656	8.16003	5.47790
B12	0.400	1.444	1.85018	2.52779	2.78786	5.17196	2.05616	5.23110	10.4622	2.61555	4.57013	10.6676	7.72955	5.34501
B13	0.340	1.444	2.29855	2.68602	2.96781	6.03569	2.28203	6.27108	12.5422	3.13554	5.00597	10.1890	6.99623	5.25323

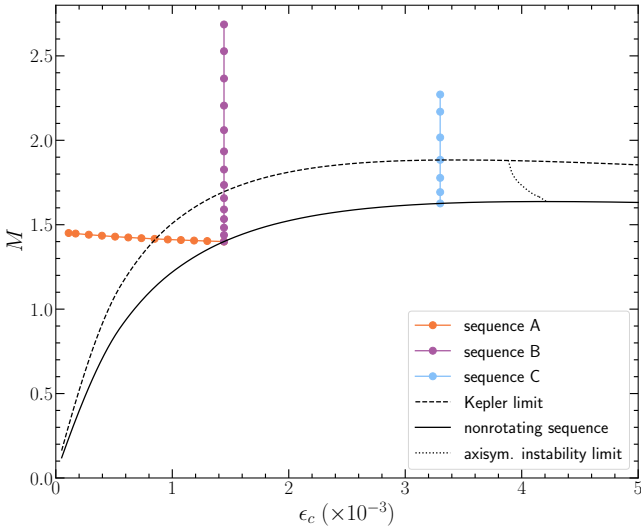


Figure 2. Gravitational mass M vs. central energy density ϵ_c for sequences A, B and C. In addition, the nonrotating (TOV) sequence (solid line), the mass-shedding (Kepler) limit for uniform rotation (dashed line) and the axisymmetric instability limit for uniform rotation (dotted line) are shown.

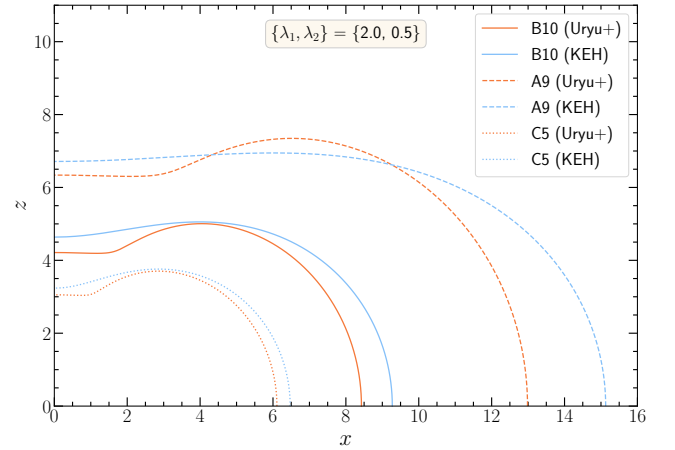


Figure 3. Stellar surfaces comparison between the Uryu+ and the KEH differential rotation laws, for representative models of each sequence with ratio $r_p/r_e \sim 0.5$. Model A9 has the same central energy density value ϵ_c for both rotation law runs, but different r_p/r_e values (0.5133 for the KEH law and 0.4882 for the Uryu+ law). This is necessary, so that the constant rest mass requirement of sequence A is satisfied accurately for both rotation laws.

3.2 Comparison to corresponding KEH sequences

Figure 3 shows a comparison of the stellar surfaces for representative models of each sequence with an r_p/r_e ratio of ~ 0.5 , between the

method by Friedman et al. (1988), see also models S1-S4 in (Baiotti et al. 2005, Table I).

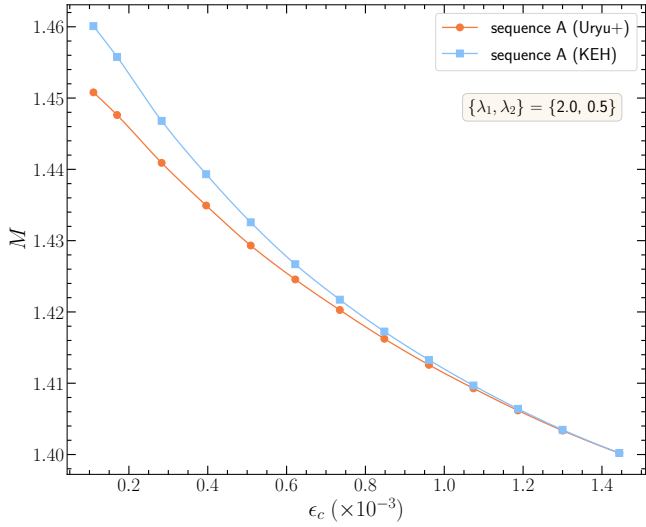


Figure 4. Comparison of gravitational mass M vs. central energy density ϵ_c for the equilibrium models of sequence A, constructed with the Uryu+ and the KEH differential rotation laws.

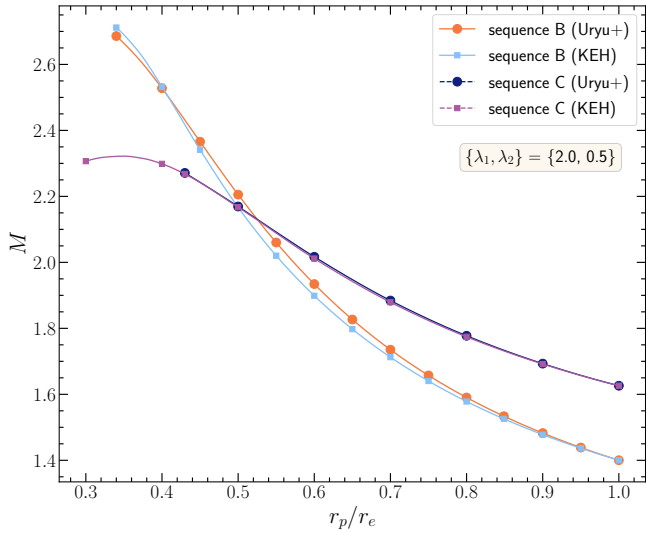


Figure 5. Comparison of gravitational mass M vs. axis ratio r_p/r_e for the equilibrium models of sequences B and C, constructed with the Uryu+ and the KEH differential rotation laws (additional intermediate models were used for sequence C, in order to display a smooth line).

Uryu+ differential rotation law and the KEH law. The Uryu+ models have a smaller radius and the surface near the rotation axis has a stronger quasi-toroidal shape than the corresponding KEH models. Note that, *based on the density distribution in the equatorial plane*, model A9 would be classified as quasi-spherical for the KEH law with $r_p/r_e = 0.5133$ and marginally quasi-toroidal for the Uryu+ law with $r_p/r_e = 0.4882$, whereas model B10 ($r_p/r_e = 0.5$) would be quasi-spherical for KEH and quasi-toroidal for the Uryu+ law and model C5 ($r_p/r_e = 0.5$) would be classified as quasi-toroidal for both rotation laws. The adoption of the Uryu+ law thus has the tendency to produce quasi-toroidal models earlier along a sequence of equilibrium models that starts at the nonrotating sequence.

Figures 4 and 5 show a comparison of the gravitational mass M

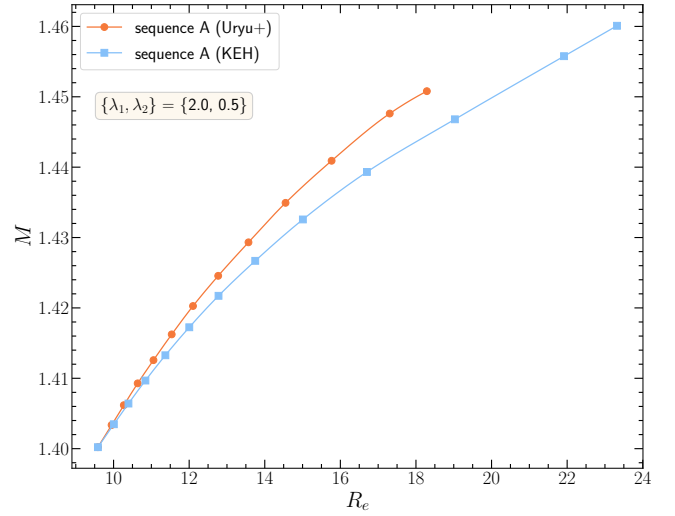


Figure 6. Comparison of gravitational mass M vs. circumferential radius R_e for the equilibrium models of sequence A, constructed with the Uryu+ and the KEH differential rotation laws.

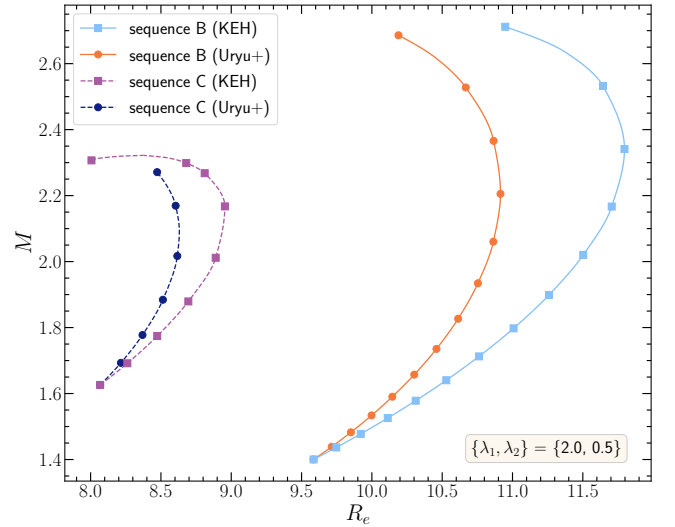


Figure 7. Comparison of gravitational mass M vs. circumferential radius R_e for the equilibrium models of sequences B and C, constructed with the Uryu+ and the KEH differential rotation laws (additional intermediate models were used, in order to display smooth lines).

along the three equilibrium sequences A, B and C, for models constructed with the Uryu+ and KEH differential rotation laws. Data for the relative physical quantities for the KEH law, appear in [Stergioulas et al. \(2004\)](#); [Iosif & Stergioulas \(2014\)](#). We find that the difference in gravitational mass between the two rotation laws is very small, for all three sequences, when one interchanges the two rotation laws.

Figures 6 and 7 compare the mass-radius relations for the three sequences A, B and C, constructed with the two rotation laws. A general remark is that all models using the Uryu+ differential rotation law (14) have consistently smaller radii than their counterparts constructed with the KEH law. The relative differences are larger for the rapidly rotating, low-density models of sequence A, where they can exceed 10%. For sequence B, the relative differences in radii

between the two differential rotation laws, range from 3% to 7% for models with axis ratio between $r_p/r_e \sim 0.7$ and ~ 0.5 , respectively. For sequence C the corresponding relative differences are at the 2% and 4% levels, owing to the greater compactness of the sequence.

3.3 Variation of parameters in the rotation law

The models defined in Sec. 3.1 and explored in Sec. 3.2 were constructed with the specific choice of $p = 1, q = 3$ and $\lambda_1 = 2.0, \lambda_2 = 0.5$. Here, we explore the impact of varying λ_1 and λ_2 , while keeping $p = 1, q = 3$ fixed, by first focusing on selected equilibrium models from each sequence with $r_p/r_e \sim 0.7$ and ~ 0.5 . Table 3 summarises our results for representative models of sequences A and B with axis ratio values of 0.7 and 0.5, while full sequence C variations are explored in Table 4. We pick two values for the first parameter $\lambda_1 = \{2.0, 1.5\}$ and two values for the second parameter $\lambda_2 = \{0.5, 1.0\}$, leading to four distinct pairs of (λ_1, λ_2) . This is motivated by the differences in rotational profiles seen in numerical simulations of post-merger remnants, when different EOS and total masses are used, see the examples in Hanauske et al. (2017); De Pietri et al. (2020).

Models A5, B6 in Table 3, and C3 in Table 4 have $r_p/r_e \sim 0.7$. Between the different $\{\lambda_1, \lambda_2\}$ runs, we notice variations in all the equilibrium quantities. The most striking difference is the fact that the equatorial radii are increasing with decreasing λ_1 and increasing λ_2 . Increasing $\lambda_2 = \Omega_e/\Omega_c$ leads to a larger radius increase, compared to the corresponding increase in radius when $\lambda_1 = \Omega_{\max}/\Omega_c$ decreases.

Models A9, B10 in Table 3 and C5 in Table 4 have $r_p/r_e \sim 0.5$. The increase of the equatorial radii with decreasing λ_1 and with increasing λ_2 is also present here, with the effect magnified due to the faster rotation. Again, increasing $\lambda_2 = \Omega_e/\Omega_c$ leads to a larger radius increase, compared to the corresponding increase in radius when $\lambda_1 = \Omega_{\max}/\Omega_c$ decreases. The difference in masses (both gravitational and rest mass) between the different $\{\lambda_1, \lambda_2\}$ runs, is more pronounced in the low-density configuration A9 compared to the other two models B10 and C5 that are more compact. An important observation is that while these models are quasi-toroidal for the choice $\{\lambda_1, \lambda_2\} = \{2.0, 0.5\}$, they are quasi-spherical for the other three $\{\lambda_1, \lambda_2\}$ options we consider here (since $\epsilon_c = \epsilon_{\max}$).

In Figure 8 we present the effect of the different λ_1 and λ_2 options on the energy density and angular velocity profiles in the equatorial plane, for the three models A9, B10 and C5 with $r_p/r_e \sim 0.5$.³ The figures in the left column of Figure 8 show the energy density profile $\epsilon(r)$ for the four different $\{\lambda_1, \lambda_2\}$ pairs considered. As we already pointed out, apart from the default option $\{\lambda_1, \lambda_2\} = \{2.0, 0.5\}$ that yields quasi-toroidal configurations for models A9, B10 and C5, the other three $\{\lambda_1, \lambda_2\}$ pairs result in quasi-spherical configurations for the same ϵ_c and r_p/r_e values. The figures in the right column of Figure 8 show the corresponding angular velocity profile $\Omega(r)$ for the four distinct $\{\lambda_1, \lambda_2\}$ pairs for each of the three chosen models, demonstrating in essence the different degrees of differential rotation considered. We notice that any choice other than the default $\{\lambda_1, \lambda_2\} = \{2.0, 0.5\}$, results in larger radii, with respect to this choice.

In order to probe whether the morphology of the selected models A9, B10 and C5 falls into the spheroidal or quasi-toroidal category, we kept each model's central energy density fixed and constructed

additional configurations at lower axis ratios for each of the four pairs $\{\lambda_1, \lambda_2\}$ under study. For the three values of central energy density considered (i.e. model A9's $\epsilon_c = 0.396 \times 10^{-3}$, model B10's $\epsilon_c = 1.444 \times 10^{-3}$ and model C5's $\epsilon_c = 3.3 \times 10^{-3}$) we found that both $\{\lambda_1, \lambda_2\}$ variations with $\lambda_2 = 0.5$ (i.e. the pairs $\{2.0, 0.5\}$ and $\{1.5, 0.5\}$) exhibited strong quasi-toroidal characteristics at axis ratios lower than 0.5. Respectively, both $\{\lambda_1, \lambda_2\}$ variants with $\lambda_2 = 1.0$ (i.e. the pairs $\{2.0, 1.0\}$ and $\{1.5, 1.0\}$) came gradually closer to the mass-shedding limit, as the axis ratio was reduced below 0.5, while remaining quasi-spherical. This behaviour is reminiscent of different types of solutions in the Ansorg et al. (2009) classification scheme (where four different types of solutions, A, B, C and D were identified) and encourages a more thorough investigation of variants of complete sequences of models with different $\{\lambda_1, \lambda_2\}$ options, which we provide in the following Section.

3.4 Identification of type A and C solutions

Having performed an initial exploration for selected equilibrium models, of the effect that different values for the parameters $\{\lambda_1, \lambda_2\}$ have, we now construct variants of the complete sequence C, employing four different pairs of $\{\lambda_1, \lambda_2\}$. Our results for the four variants are reported in Table 4.

For the cases of $\{\lambda_1, \lambda_2\} = \{1.5, 1.0\}$ and $\{2.0, 1.0\}$ we find that the sequence reaches the mass-shedding limit (where $\Omega_e = \Omega_K$) at an axis ratio r_p/r_e of 0.46693 and 0.38602, correspondingly. From Table 4, we notice that these models at the mass-shedding limit are still quasi-spherical ($\epsilon_c = \epsilon_{\max}$). The lower panels of Figure 9 show that the two-dimensional rest-mass density distributions of these two models at the mass-shedding limit feature the characteristic cusp in the equatorial plane. In addition, the lower panels of Figure 10 show the shape of the surface for all members of the two variants of sequence C that terminate at the mass-shedding limit. Evidently, these two variants of sequence C remain quasi-spherical, up to mass-shedding. We conclude that the variants of sequence C calculated with $\{\lambda_1, \lambda_2\} = \{1.5, 1.0\}$ and $\{\lambda_1, \lambda_2\} = \{2.0, 1.0\}$ can be classified as type A solutions⁴, according to the classification of Ansorg et al. (2009).

For the variant of sequence C with $\{\lambda_1, \lambda_2\} = \{2.0, 0.5\}$, quasi-toroidal models appear already at $r_p/r_e = 0.5$ (see Table 4, where for model C5 of this variation, $\epsilon_c < \epsilon_{\max}$, i.e. the maximum density is off-center). The upper left panel of Figure 9 shows the meridional rest mass density distribution for the terminal model of this variation (model C6 with $r_p/r_e = 0.43$). The corresponding panel of Figure 10 shows that the shape of the surface for the members of this sequence is transitioning from quasi-spheroidal models at high axis ratio to quasi-toroidal models at low axis ratio. Since the mass-shedding limit has not been reached (see Table 4), even though the models have become quasi-toroidal, we classify the models belonging to this variant of sequence C as type C solutions⁵, following Ansorg et al. (2009).

For the variant of sequence C with $\{\lambda_1, \lambda_2\} = \{1.5, 0.5\}$ the situation is similar to the case of $\{\lambda_1, \lambda_2\} = \{2.0, 0.5\}$. After constructing the initial quasi-spheroidal models of this family (i.e. models with $r_p/r_e > 0.5$ where $\epsilon_c = \epsilon_{\max}$, see Table 4) we performed a search starting from an axis ratio value of 0.5 and decreased r_p/r_e using a

³ Depending on the cut-off density, the EOS and the total mass, the axis ratio r_p/r_e of post-merger remnants in simulations is roughly in the range between ~ 0.5 and ~ 0.7 .

⁴ We caution that our terminology of "sequence A" should not be confused with the terminology of "type A solutions".

⁵ We caution that our terminology of "sequence C" should not be confused with the terminology of "type C solutions".

Table 3. Comparison of the properties of selected equilibrium models constructed with different choices of λ_1 and λ_2 , for models A5, B6 (which have $r_p/r_e \sim 0.7$) and A9, B10 (which have $r_p/r_e \sim 0.5$).

$\{\lambda_1, \lambda_2\}$	ϵ_{\max} ($\times 10^{-3}$)	M	M_0	J	$T/ W $ ($\times 10^{-1}$)	Ω_c ($\times 10^{-2}$)	Ω_{\max} ($\times 10^{-2}$)	Ω_e ($\times 10^{-2}$)	Ω_K ($\times 10^{-2}$)	R_e	r_e	GRV3 ($\times 10^{-5}$)
A5												
{2.0, 0.5}	0.84800	1.41624	1.50599	1.17284	0.80274	1.97572	3.95145	0.98786	3.08876	11.5380	10.0283	6.47831
{1.5, 0.5}	0.84800	1.41101	1.49924	1.22732	0.83749	2.14216	3.21324	1.07108	3.00473	11.7518	10.2458	6.51115
{2.0, 1.0}	0.84800	1.38326	1.46668	1.26335	0.87340	1.26841	2.53681	1.26841	2.79005	12.2995	10.8216	6.56797
{1.5, 1.0}	0.84800	1.34909	1.42915	1.17292	0.80248	1.44535	2.16802	1.44535	2.67567	12.5382	11.1014	6.58230
A9												
{2.0, 0.5}	0.40086	1.43493	1.50612	1.96591	1.64514	1.97549	3.95098	0.98775	2.28329	14.5499	12.9843	6.03066
{1.5, 0.5}	0.39600	1.40917	1.47544	2.05700	1.75397	2.04435	3.06653	1.02218	2.11360	15.2859	13.7453	6.06753
{2.0, 1.0}	0.39600	1.23786	1.28617	1.84376	1.84378	1.04896	2.09792	1.04896	1.60791	17.6713	16.3254	5.72760
{1.5, 1.0}	0.39600	0.95152	0.98436	0.91411	1.17554	1.07258	1.60887	1.07258	1.16908	19.5914	18.5953	5.17216
B6												
{2.0, 0.5}	1.44400	1.73532	1.88009	1.70054	0.89312	2.76602	5.53204	1.38301	3.91929	10.4592	8.57816	6.38871
{1.5, 0.5}	1.44400	1.73978	1.88364	1.80491	0.93770	2.97529	4.46294	1.48765	3.79636	10.7057	8.81697	6.49973
{2.0, 1.0}	1.44400	1.72067	1.85873	1.88673	0.97554	1.72430	3.44860	1.72430	3.48046	11.3380	9.46891	6.63232
{1.5, 1.0}	1.44400	1.67444	1.80673	1.73283	0.88100	1.93610	2.90414	1.93610	3.30765	11.6248	9.81449	6.71866
B10												
{2.0, 0.5}	1.48092	2.20535	2.41490	3.63795	1.65695	4.10748	8.21495	2.05374	4.15491	10.9145	8.42730	5.64007
{1.5, 0.5}	1.44400	2.25934	2.47226	4.08241	1.77762	4.19581	6.29371	2.09790	3.85379	11.6077	9.05178	5.50127
{2.0, 1.0}	1.44400	2.16091	2.34520	4.10365	1.79888	2.03625	4.07251	2.03625	2.92086	13.8811	11.4650	5.75583
{1.5, 1.0}	1.44400	1.79857	1.94018	2.41485	1.18892	2.03940	3.05909	2.03940	2.27672	15.3167	13.3840	5.82863

0.01 step. We noticed a local maximum in the energy density profile at the equatorial plane gradually rising and when the axis ratio reached the value 0.41, the maximum density was found to be definitively off-center. This marked the transition to quasi-toroidal configurations. We kept on decreasing the axis ratio, down to a value of 0.31, where the rns code ceased producing models for this choice of parameters. The upper right panel of Figure 9 shows the meridional rest mass density distribution for the terminal model C9 (with $r_p/r_e = 0.31$). Models constructed with $0.41 > r_p/r_e \geq 0.31$ exhibited a gradually “stronger” quasi-toroidal morphology (see upper right panel of Figure 10), while Ω_e always remained smaller than Ω_K . We note that for the terminal model C9, we have $\Omega_e/\Omega_K \simeq 0.77$, i.e. no mass-shedding limit is encountered. Thus, we classify the variant of sequence C, calculated with $\{\lambda_1, \lambda_2\} = \{1.5, 0.5\}$, as a type C solution, according to Ansorg et al. (2009).

We note, that as can be seen from the right column of Figure 8, the pairs $\{\lambda_1, \lambda_2\} = \{1.5, 1.0\}$ and $\{\lambda_1, \lambda_2\} = \{2.0, 1.0\}$ that yield type A solutions represent lower degrees of differential rotation compared to the pairs $\{\lambda_1, \lambda_2\} = \{2.0, 0.5\}$ and $\{\lambda_1, \lambda_2\} = \{1.5, 0.5\}$ that result in type C solutions. The pair $\{\lambda_1, \lambda_2\} = \{2.0, 0.5\}$ corresponds to the highest degree of differential rotation and the pair $\{1.5, 1.0\}$ to the lowest. This observation together with the classification of solutions described above are in agreement with Ansorg et al. (2009), where it was demonstrated that type C solutions arise for a larger degree of differential rotation, whereas type A solutions correspond to a lower degree of differential rotation.

Finally, Figure 11 further demonstrates the distinct types of solutions for the choices of $\{\lambda_1, \lambda_2\}$ considered. In the mass vs. equatorial radius plane, the four sequence C variants form a “bouquet” of equilibrium sequences where type A solutions are clearly distinguished from type C solutions. The sequences with type A solutions have a monotonically increasing radius and exhibit a maximum mass. In

contrast, the sequences with type C solutions have a monotonically increasing mass and exhibit a maximum radius (which is significantly smaller than the radius of most type A models). A more detailed investigation of sequences with different $\{\lambda_1, \lambda_2\}$ values may reveal the location of a separatrix in between the two types of solutions.

We note that the variation of λ_2 appears to have the strongest effect regarding the type of solutions: keeping λ_1 constant and varying λ_2 from 0.5 to 1.0, results to a transition from type C to type A solutions (observe Figure 10 per column of panels), whereas if we keep λ_2 fixed and vary λ_1 from 2.0 to 1.5 the type of solution remains the same (observe Figure 10 per row of panels). The above observations hold for the particular values of $\{p, q\} = \{1, 3\}$ of the Uryu+ rotation law (14) that are kept fixed within the scope of this work.

4 SUMMARY AND CONCLUSIONS

In this work, our goal was to investigate the new 4-parameter differential rotation law (14) introduced in Uryū et al. (2017), as a more realistic option compared to the classic j -constant law (13) for describing compact remnants from BNS mergers, in quasi-equilibrium. We did this by constructing sequences of equilibrium models, that can be used as reference models to compare with different rotation law implementations. We found that the new 4-parameter rotation law provides much more versatility as a candidate for equilibrium model building. The Uryu+ law constitutes essentially an upgrade from the widely used KEH, as it comes much closer to the angular velocity profile of merger remnants (as seen in a plethora of numerical simulations) and at the same time, it can produce models with an axis ratio between ~ 0.5 and ~ 0.7 for which the models are quasi-spherical (as defined by the energy density profile in the equatorial plane).

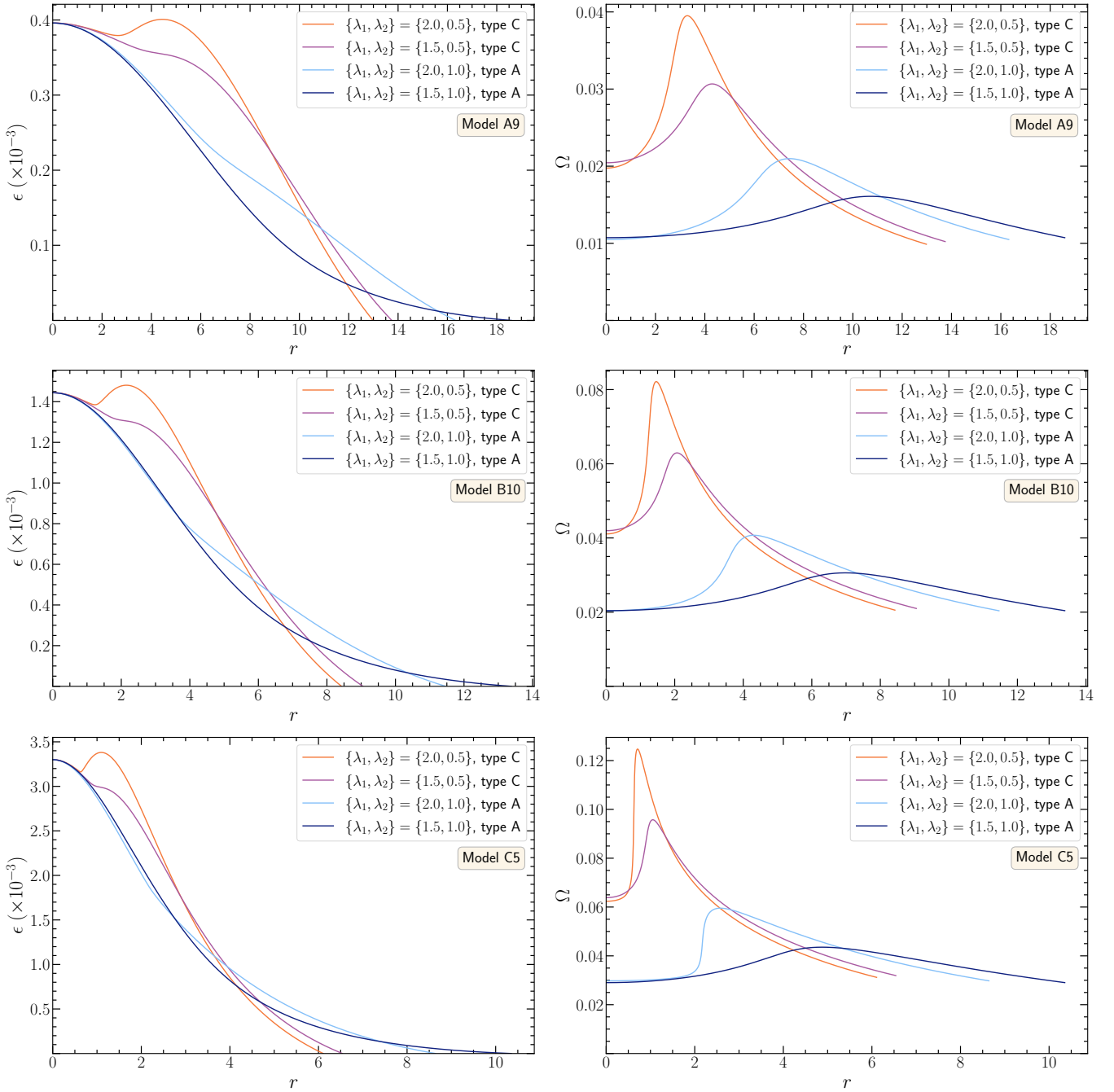


Figure 8. *Left column:* Effect of different options for $\{\lambda_1, \lambda_2\}$ on the energy density profile $\epsilon(r)$ versus the coordinate radius r , in the equatorial plane for models A9 ($r_p/r_e = 0.4882$), B10 ($r_p/r_e = 0.5$) and C5 ($r_p/r_e = 0.5$). *Right column:* Same as left column, but for the angular velocity profile $\Omega(r)$ in the equatorial plane.

Since the work of Uryū et al. (2017) there has been a shortage of reference models constructed with the newly proposed rotation laws. The original work of Uryū et al. focused on presenting a limited number of selected models. Subsequent studies used the new 4-parameter Uryu+ rotation law for describing rotating strange stars (Zhou et al. 2019), explored the new 3-parameter Uryu+ rotation law in a Newtonian framework (Passamonti & Andersson 2020), and evolved in GR a selected model constructed with the new 3-parameter Uryu+ rotation law (Xie et al. 2020). This was a gap that we tried

to partially fill, for the case of the new 4-parameter Uryu+ rotation law, with our present contribution. Expanding the well-tested, robust and fully relativistic, numerical code rns with the newly suggested rotation law, provides an additional testing platform, thus supporting the further development of more realistic rotation laws.

Specifically, building on Uryū et al. (2017), the implicit treatment of parameters A and B through the ratios λ_1 and λ_2 , allows one to easily take advantage of information provided from numerical simulations in order to fine-tune the parameter values of the rotation

Table 4. Physical quantities for variations of sequence C (with constant $\epsilon_c = 3.3 \times 10^{-3}$) calculated using the Uryu+ differential rotation law (14) and four different $\{\lambda_1, \lambda_2\}$ choices. The different quantities are defined as in Table 1.

Model $\{\lambda_1, \lambda_2\}$	r_p/r_e	ϵ_c ($\times 10^{-3}$)	ϵ_{\max} ($\times 10^{-3}$)	M	M_0	J	$T/ W $ ($\times 10^{-1}$)	Ω_c ($\times 10^{-2}$)	Ω_{\max} ($\times 10^{-2}$)	Ω_e ($\times 10^{-2}$)	Ω_K ($\times 10^{-2}$)	R_e	r_e	GRV3 ($\times 10^{-5}$)
C0	1.0	3.300	3.30000	1.62609	1.78404	0.0	0.0	0.0	0.0	0.0	5.56489	8.06761	6.33721	4.07290
{2.0, 0.5}														
C1	0.900	3.300	3.30000	1.69308	1.85770	0.82658	0.26133	2.21234	4.42469	1.10617	5.45745	8.21539	6.39361	8.22374
C2	0.800	3.300	3.30000	1.77749	1.95056	1.33108	0.55526	3.24900	6.49800	1.62450	5.43431	8.36885	6.43192	7.27867
C3	0.700	3.300	3.30000	1.88427	2.06789	1.88720	0.88511	4.16835	8.33671	2.08418	5.45131	8.51392	6.43013	6.50502
C4	0.600	3.300	3.30000	2.01691	2.21281	2.55894	1.25159	5.11713	10.2343	2.55856	5.53276	8.61636	6.34583	5.92909
C5	0.500	3.300	3.38103	2.16935	2.37578	3.36450	1.64806	6.23604	12.4721	3.11802	5.73080	8.60458	6.10795	5.50829
C6	0.430	3.300	3.78169	2.27114	2.47788	3.95736	1.93348	7.22363	14.4473	3.61181	5.97797	8.47292	5.81060	5.31201
{1.5, 0.5}														
C1	0.900	3.300	3.30000	1.69744	1.86262	0.87469	0.27516	2.43702	3.65552	1.21851	5.41157	8.26711	6.43940	8.41869
C2	0.800	3.300	3.30000	1.78925	1.96400	1.42246	0.58641	3.53712	5.30569	1.76856	5.33519	8.49234	6.53988	7.63975
C3	0.700	3.300	3.30000	1.90963	2.09728	2.04905	0.93923	4.46770	6.70156	2.23385	5.28216	8.74006	6.62358	6.92976
C4	0.600	3.300	3.30000	2.06929	2.27439	2.85553	1.33838	5.37174	8.05761	2.68587	5.26961	8.99051	6.65339	6.26718
C5	0.500	3.300	3.30000	2.27675	2.50393	3.93817	1.78309	6.38320	9.57480	3.19160	5.35024	9.17495	6.54069	5.65454
C6	0.450	3.300	3.30000	2.39419	2.63214	4.58693	2.01748	6.99955	10.4993	3.49977	5.45900	9.19236	6.38077	5.39346
C7	0.400	3.300	3.37195	2.50860	2.75322	5.25894	2.25273	7.74559	11.6184	3.87280	5.63695	9.12106	6.12492	5.19915
C8	0.350	3.300	3.78944	2.60300	2.84493	5.86720	2.48126	8.65126	12.9769	4.32563	5.88738	8.95023	5.78398	5.11267
C9	0.310	3.300	4.25504	2.65527	2.88547	6.25344	2.65580	9.47333	14.2101	4.73666	6.11700	8.76773	5.49073	5.14309
{2.0, 1.0}														
C1	0.900	3.300	3.30000	1.70172	1.86729	0.93253	0.29149	1.49441	2.98881	1.49441	5.29985	8.39149	6.55728	8.57625
C2	0.800	3.300	3.30000	1.79926	1.97507	1.52450	0.61561	2.10463	4.20927	2.10463	5.08468	8.79815	6.83195	7.86928
C3	0.700	3.300	3.30000	1.92722	2.11714	2.20949	0.97340	2.54465	5.08929	2.54465	4.83450	9.32979	7.19275	7.22397
C4	0.600	3.300	3.30000	2.09626	2.30584	3.09888	1.35888	2.85349	5.70699	2.85349	4.51125	10.0721	7.71297	6.72010
C5	0.500	3.300	3.30000	2.30708	2.54232	4.26788	1.73331	2.97673	5.95346	2.97673	4.01493	11.2684	8.64295	6.30155
C6	0.450	3.300	3.30000	2.39295	2.63801	4.80388	1.84621	2.88492	5.76984	2.88492	3.58163	12.3292	9.61201	6.08501
C7	0.400	3.300	3.30000	2.22585	2.44598	3.95290	1.53164	2.47488	4.94977	2.47488	2.68011	14.6073	12.1649	6.28917
C8	0.38602	3.300	3.30000	2.02169	2.21845	2.79739	1.13836	2.26348	4.52696	2.26348	2.26353	15.7686	13.6103	6.60086
{1.5, 1.0}														
C1	0.900	3.300	3.30000	1.69717	1.86235	0.91215	0.27301	1.71448	2.57171	1.71448	5.24254	8.44636	6.61807	8.63909
C2	0.800	3.300	3.30000	1.78461	1.95901	1.46353	0.56461	2.37684	3.56526	2.37684	4.94888	8.93946	6.99342	8.02860
C3	0.700	3.300	3.30000	1.88878	2.07452	2.04385	0.86078	2.80492	4.20738	2.80492	4.57924	9.61981	7.53786	7.47561
C4	0.600	3.300	3.30000	1.99392	2.19113	2.62218	1.11124	3.01744	4.52616	3.01744	4.05461	10.6529	8.44373	7.01096
C5	0.500	3.300	3.30000	1.99260	2.18826	2.64193	1.08973	2.90352	4.35528	2.90352	3.18093	12.5257	10.3560	6.79391
C6	0.490	3.300	3.30000	1.97350	2.16693	2.53802	1.04493	2.86533	4.29799	2.86533	3.06002	12.8046	10.6660	6.79974
C7	0.480	3.300	3.30000	1.94882	2.13949	2.40167	0.98693	2.82147	4.23221	2.82147	2.93199	13.1080	11.0081	6.83711
C8	0.46693	3.300	3.30000	1.90861	2.09501	2.17639	0.89089	2.75619	4.13429	2.75619	2.75620	13.5436	11.5046	6.86623

law. For example, according to recent simulations (Hanauske et al. 2017; De Pietri et al. 2020), a value of $\lambda_2 = 1$ could be favoured over $\lambda_2 = 0.5$, for the case of compact remnants from BNS mergers, while λ_1 falls in a range between 1.7-1.9 for realistic EOS. Furthermore, we also found that using different λ_1 and λ_2 values can have an impact on whether the constructed configuration's morphology is quasi-spherical or quasi-toroidal.

Going beyond the characterization of selected equilibrium models, we constructed variants of complete sequence with different $\{\lambda_1, \lambda_2\}$ options, which reflect the different degrees of differential rotation considered. For two of these choices, namely $\{1.5, 1.0\}$ and $\{2.0, 1.0\}$, we were able to find a mass-shedding limit for the new Uryu+ rotation law, which identifies the corresponding sequences as type A solutions, according to the classification in Ansorg et al. (2009). The other two choices, namely $\{2.0, 0.5\}$ and $\{1.5, 0.5\}$, result in families of models consisting of both quasi-spheroidal and quasi-toroidal configurations, for which no mass-shedding was en-

countered. We identified the corresponding sequences as type C solutions, in the Ansorg et al. (2009) classification. Zhou et al. (2019) also explored type C solutions for the case of strange stars with the 4-parameter Uryu+ law (14). Here, we present the first classification of *different* types of solutions (A and C) with a rotation law other than the KEH law used in Ansorg et al. (2009).

A more thorough exploration of the parameter space for all four parameters $\{p, q, \lambda_1, \lambda_2\}$ of the Uryu et al. (2017) law will be required to investigate the possible existence of other types of solutions (which are called type B and type D in the classification of Ansorg et al. 2009).

Another result to highlight is the fact that, as shown in Figure 7, we systematically obtained smaller radii for our Uryu+ models compared to the corresponding KEH models. For models with $r_p/r_e > 0.45$ this can be explained by the fact that, with the Uryu+ law, the angular velocity at the equator, Ω_e is smaller than for the corresponding

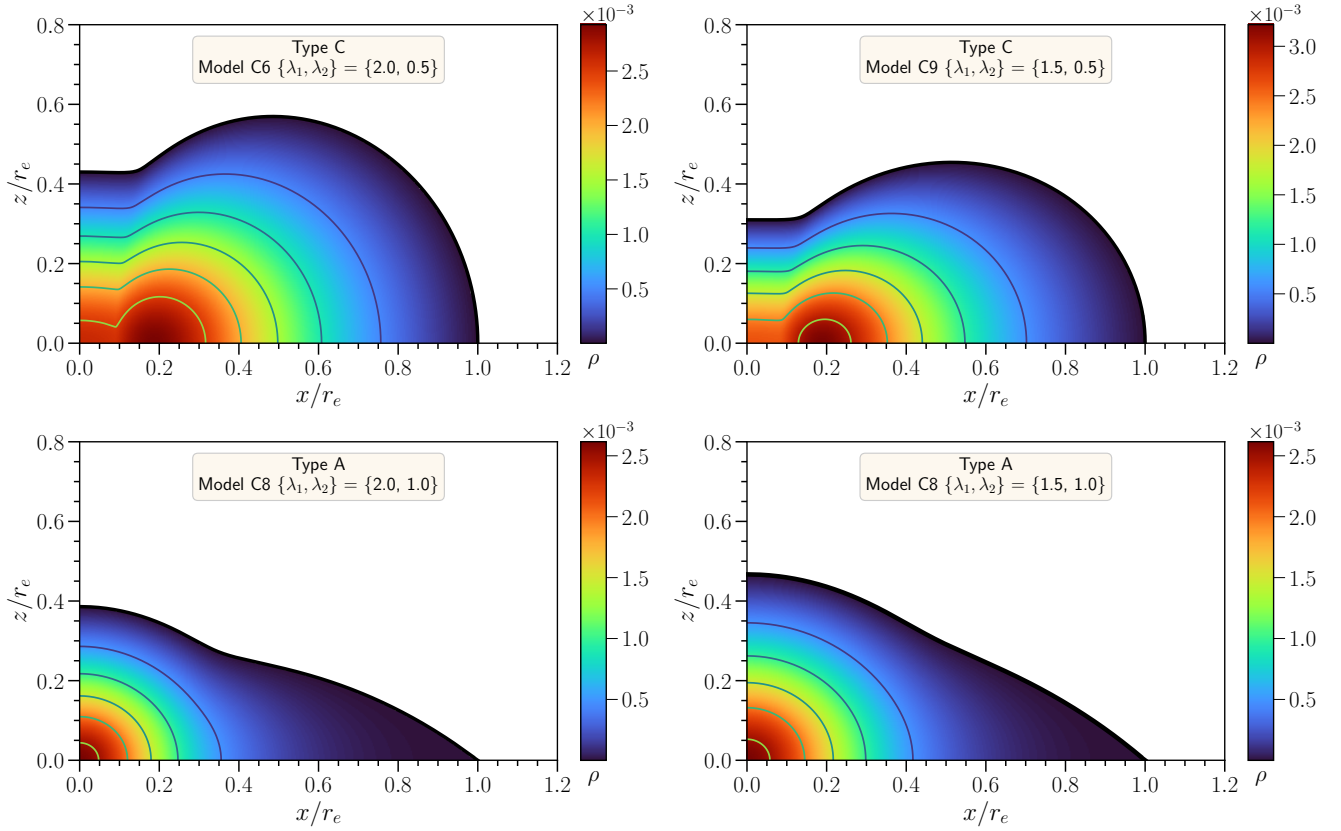


Figure 9. Two-dimensional rest mass density distribution ρ (in dimensionless units $c = G = M_\odot = 1$) for the terminal models of each variation of sequence C for the different $\{\lambda_1, \lambda_2\}$ pairs employed (see Table 4). The solid black curves represent the models' surfaces. The coordinates x and z are rescaled with each model's coordinate radius at the equator r_e . The mass-shedding limit is encountered for $\{\lambda_1, \lambda_2\} = \{2.0, 1.0\}$ at $r_p/r_e = 0.38602$ and for $\{\lambda_1, \lambda_2\} = \{1.5, 1.0\}$ at $r_p/r_e = 0.46693$, meaning sequence C belongs to type A solutions (Ansorg et al. 2009) for these choices of parameters. No mass-shedding limit is found for $\{\lambda_1, \lambda_2\} = \{2.0, 0.5\}$, where the terminal model C6 is reached at $r_p/r_e = 0.43$ and $\{\lambda_1, \lambda_2\} = \{1.5, 0.5\}$, where the terminal model C9 is reached at $r_p/r_e = 0.31$. The appearance of quasi-toroidal models characterizes these variations of sequence C as type C solutions according to Ansorg et al..

models with the KEH law, resulting in a weaker centrifugal force and thus in a smaller radius.

In Appendix B, we investigate the impact of the spatially, conformally flat, spacetime approximation IWM-CFC (Isenberg 2008; Wilson et al. 1996) on the equilibrium structure of models built with the Uryu+ rotation law. We show that down to an axis ratio of $r_p/r_e \sim 0.5$ (which is typical for post-merger remnants), the error introduced by the IWM-CFC approximation remains relatively small.

We point out, that in some recent simulations of BNS mergers a large effective viscosity was used (as a model for the turbulent viscosity due to the magneto-rotational instability, MRI), resulting in a rotational profile that quickly becomes uniformly rotating in most parts of the remnant (see Shibata et al. 2017; Shibata & Kiuchi 2017; Radice 2017; Fujibayashi et al. 2018). Whether current simulations have sufficient resolution to accurately inform us about the timescale of the development of the MRI instability remains to be seen (see Kiuchi et al. 2018; Cioffi 2020; Radice 2020).

In future work, we aim to expand this initial study from $N = 1$ polytropes to tabulated and hot EOS. The inclusion of thermal effects (Kaplan et al. 2014; Camelio et al. 2019) is important to allow for a more realistic reconstruction of post-merger remnants as quasi-equilibrium models, see Camelio et al. (2020). In addition, we also plan to study the dynamics of equilibrium models built with the Uryu+ differential rotation law, by investigating their oscillation

modes and the onset of the low $T/|W|$ instabilities in models (see Passamonti & Andersson 2020; Xie et al. 2020).

The rotational properties of binary neutron star merger remnants have important astrophysical consequences, affecting e.g. the precise thresholds to prompt or delayed collapse to a black hole (with further consequences on the development of a possible short gamma-ray burst, observable in the electromagnetic spectrum, see e.g. the reviews by Bauswein & Stergioulas (2019); Friedman & Stergioulas (2020) and references therein). The semi-analytic derivation of an empirical relation for the threshold mass of Bauswein & Stergioulas (2017) could be updated, using the new rotation law and tabulated EOS. It will also be worth to investigate quasi-universal relations, such as those presented in Bozzola et al. (2018); Weih et al. (2018), using the new rotation law.

ACKNOWLEDGEMENTS

We are grateful to the anonymous referee for useful comments that significantly improved the final version of the manuscript. We also thank Gabriele Bozzola and Wolfgang Kastaun for useful discussions and Giovanni Camelio, Tim Dietrich, Stephan Rosswog and Bryn Haskell for advanced sharing of a manuscript on a related topic and for comments on our manuscript. PI gratefully acknowledges support by a Virgo-EGO Scientific Forum (VESF) PhD fellowship.

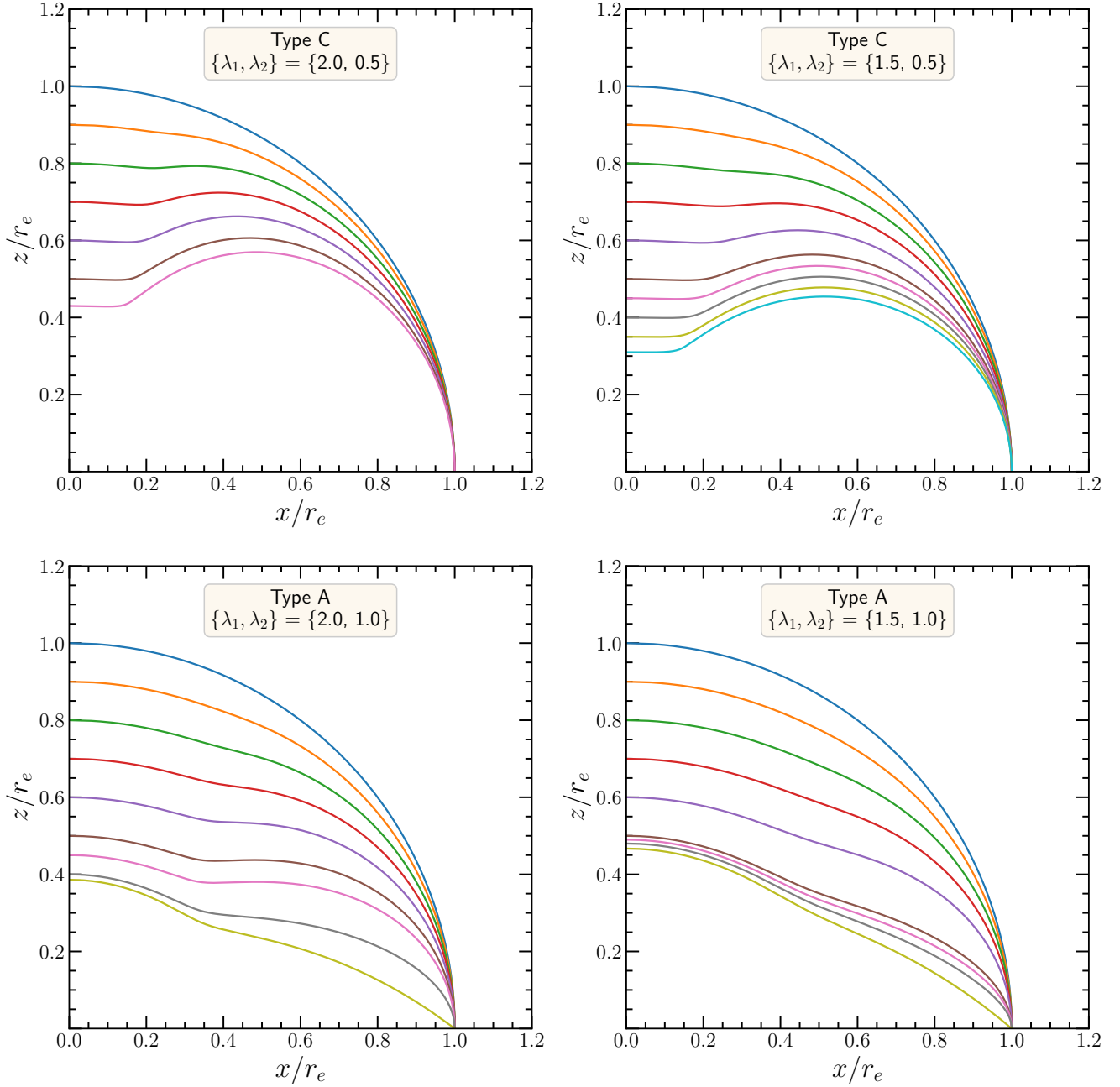


Figure 10. Surface shape for all variations of sequence C for the different $\{\lambda_1, \lambda_2\}$ pairs employed (see Table 4). The coordinates x and z are rescaled with each model's coordinate radius at the equator r_e . The different colors in each panel represent the different models of each variation of sequence C, as reported in Table 4. The upper panels represent type C solutions according to the classification of Ansorg et al. (2009) for values $\{\lambda_1, \lambda_2\} = \{2.0, 0.5\}$ and $\{\lambda_1, \lambda_2\} = \{1.5, 0.5\}$, while the lower panels represent type A solutions for values $\{\lambda_1, \lambda_2\} = \{2.0, 1.0\}$ and $\{\lambda_1, \lambda_2\} = \{1.5, 1.0\}$.

The authors gratefully acknowledge the Italian Istituto Nazionale di Fisica Nucleare (INFN), the French Centre National de la Recherche Scientifique (CNRS) and the Netherlands Organization for Scientific Research, for the construction and operation of the Virgo detector and the creation and support of the EGO consortium.

DATA AVAILABILITY

The data underlying this article are available in the article.

REFERENCES

- Abbott B. P., et al., 2017a, *Phys. Rev. Lett.*, 119, 161101
- Abbott B. P., et al., 2017b, *ApJL*, 848, L13
- Ansorg M., Gondek-Rosińska D., Villain L., 2009, *MNRAS*, 396, 2359
- Baiotti L., Hawke I., Montero P. J., Löffler F., Rezzolla L., Stergioulas N., Font J. A., Seidel E., 2005, *Phys. Rev. D*, 71, 024035
- Baumgarte T. W., Shapiro S. L., Shibata M., 2000, *ApJ*, 528, L29
- Bauswein A., Janka H. T., 2012, *Phys. Rev. Lett.*, 108, 011101
- Bauswein A., Stergioulas N., 2015, *Phys. Rev. D*, 91, 124056
- Bauswein A., Stergioulas N., 2017, *MNRAS*, 471, 4956
- Bauswein A., Stergioulas N., 2019, *J. Phys. G: Nucl. Part. Phys.*, 46, 113002

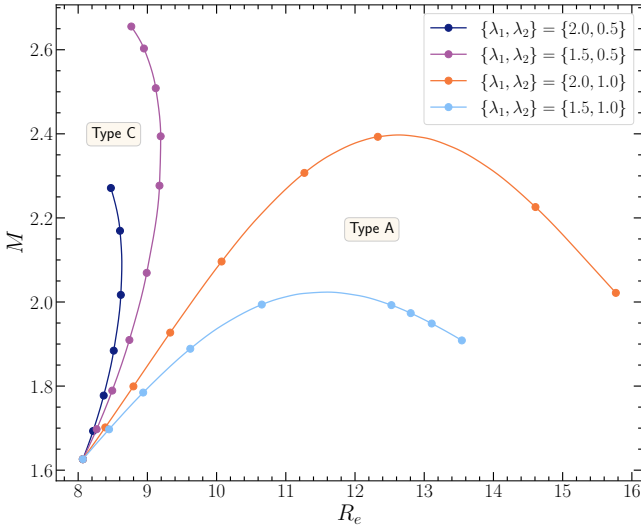


Figure 11. Comparison of gravitational mass M vs. circumferential radius R_e for the variations of sequence C, constructed with the Uryu+ differential rotation law and employing different $\{\lambda_1, \lambda_2\}$ values (see Table 4). Equilibrium models with $\{\lambda_1, \lambda_2\} = \{2.0, 0.5\}$ and $\{1.5, 0.5\}$ are type C solutions, while models with $\{\lambda_1, \lambda_2\} = \{2.0, 1.0\}$ and $\{1.5, 1.0\}$ are type A solutions according to Ansorg et al. (2009) (additional intermediate models were used, in order to display smooth lines).

Bauswein A., Janka H. T., Hebeler K., Schwenk A., 2012, *Phys. Rev. D*, **86**, 063001

Bauswein A., Stergioulas N., Janka H.-T., 2016, *Eur. Phys. J. A*, **52**, 56

Bernuzzi S., 2020, *Gen. Relativ. Gravit.*, **52**, 108

Bernuzzi S., Dietrich T., Tichy W., Brügmann B., 2014, *Phys. Rev. D*, **89**, 104021

Bozzola G., Stergioulas N., Bauswein A., 2018, *MNRAS*, **474**, 3557

Camelio G., Dietrich T., Marques M., Rosswog S., 2019, *Phys. Rev. D*, **100**, 123001

Camelio G., Dietrich T., Rosswog S., Haskell B., 2020, arXiv e-prints, p. arXiv:2011.10557

Cioffi R., 2020, *Gen. Relativ. Gravit.*, **52**, 59

Cioffi R., Kastaun W., Giacomazzo B., Endrizzi A., Siegel D. M., Perna R., 2017, *Phys. Rev. D*, **95**, 063016

Cioffi R., Kastaun W., Kalinani J. V., Giacomazzo B., 2019, *Phys. Rev. D*, **100**, 023005

Cook G. B., Shapiro S. L., Teukolsky S. A., 1992, *ApJ*, **398**, 203

De Pietri R., Feo A., Maione F., Löffler F., 2016, *Phys. Rev. D*, **93**, 064047

De Pietri R., Feo A., Font J. A., Löffler F., Pasquali M., Stergioulas N., 2020, *Phys. Rev. D*, **101**, 064052

Dietrich T., Bernuzzi S., Ujevic M., Brügmann B., 2015, *Phys. Rev. D*, **91**, 124041

East W. E., Paschalidis V., Pretorius F., Shapiro S. L., 2016, *Phys. Rev. D*, **93**, 024011

East W. E., Paschalidis V., Pretorius F., Tsokaros A., 2019, *Phys. Rev. D*, **100**, 124042

Endrizzi A., Cioffi R., Giacomazzo B., Kastaun W., Kawamura T., 2016, *Class. Quantum Gravity*, **33**, 164001

Endrizzi A., Logoteta D., Giacomazzo B., Bombaci I., Kastaun W., Cioffi R., 2018, *Phys. Rev. D*, **98**, 043015

Espino P. L., Paschalidis V., 2019, *Phys. Rev. D*, **99**, 083017

Espino P. L., Paschalidis V., Baumgarte T. W., Shapiro S. L., 2019, *Phys. Rev. D*, **100**, 043014

Friedman J. L., Stergioulas N., 2013, *Rotating Relativistic Stars*. Cambridge Monographs on Mathematical Physics, Cambridge University Press, doi:10.1017/CBO9780511977596

Friedman J. L., Stergioulas N., 2020, *Int. J. Mod. Phys. D*, **29**, 2041015

Friedman J. L., Ipser J. R., Sorkin R. D., 1988, *ApJ*, **325**, 722

Fujibayashi S., Kiuchi K., Nishimura N., Sekiguchi Y., Shibata M., 2018, *ApJ*, **860**, 64

Galeazzi F., Yoshida S., Eriguchi Y., 2012, *A&A*, **541**, A156

Giacomazzo B., Rezzolla L., Stergioulas N., 2011, *Phys. Rev. D*, **84**, 024022

Goldstein A., et al., 2017, *ApJL*, **848**, L14

Hanauske M., Takami K., Bovard L., Rezzolla L., Font J. A., Galeazzi F., Stöcker H., 2017, *Phys. Rev. D*, **96**, 043004

Hotokezaka K., Kyutoku K., Okawa H., Shibata M., Kiuchi K., 2011, *Phys. Rev. D*, **83**, 124008

Hotokezaka K., Kiuchi K., Kyutoku K., Muranushi T., Sekiguchi Y.-i., Shibata M., Taniguchi K., 2013, *Phys. Rev. D*, **88**, 044026

Iosif P., Stergioulas N., 2014, *Gen. Relativ. Gravit.*, **46**, 1800

Isenberg J. A., 2008, *Int. J. Mod. Phys. D*, **17**, 265

Kaplan J. D., Ott C. D., O'Connor E. P., Kiuchi K., Roberts L., Duez M., 2014, *ApJ*, **790**, 19

Karkowski J., Kulczycki W., Mach P., Malec E., Odrzywolek A., Piróg M., 2018, *Phys. Rev. D*, **97**, 104017

Kastaun W., Galeazzi F., 2015, *Phys. Rev. D*, **91**, 064027

Kastaun W., Cioffi R., Giacomazzo B., 2016, *Phys. Rev. D*, **94**, 044060

Kastaun W., Cioffi R., Endrizzi A., Giacomazzo B., 2017, *Phys. Rev. D*, **96**, 043019

Kiuchi K., Kyutoku K., Sekiguchi Y., Shibata M., 2018, *Phys. Rev. D*, **97**, 124039

Komatsu H., Eriguchi Y., Hachisu I., 1989, *MNRAS*, **237**, 355

Kulczycki W., Malec E., 2020, *Phys. Rev. D*, **101**, 084016

Mach P., Malec E., 2015, *Phys. Rev. D*, **91**, 124053

Nozawa T., Stergioulas N., Gourgoulhon E., Eriguchi Y., 1998, *A&AS*, **132**, 431

Paschalidis V., Stergioulas N., 2017, *Living Rev. Relativ.*, **20**, 7

Paschalidis V., East W. E., Pretorius F., Shapiro S. L., 2015, *Phys. Rev. D*, **92**, 121502

Passamonti A., Andersson N., 2020, *MNRAS*, **498**, 5904

Radice D., 2017, *ApJL*, **838**, L2

Radice D., 2020, *Symmetry*, **12**

Radice D., Perego A., Bernuzzi S., Zhang B., 2018, *MNRAS*, **481**, 3670

Sekiguchi Y., Kiuchi K., Kyutoku K., Shibata M., 2011, *Phys. Rev. Lett.*, **107**, 051102

Shibata M., Hotokezaka K., 2019, *Annu. Rev. Nucl. Part. Sci.*, **69**, 41

Shibata M., Kiuchi K., 2017, *Phys. Rev. D*, **95**, 123003

Shibata M., Kiuchi K., Sekiguchi Y.-i., 2017, *Phys. Rev. D*, **95**, 083005

Stergioulas N., Friedman J. L., 1995, *ApJ*, **444**, 306

Stergioulas N., Apostolatos T. A., Font J. A., 2004, *MNRAS*, **352**, 1089

Stergioulas N., Bauswein A., Zagkouris K., Janka H.-T., 2011, *MNRAS*, **418**, 427

Takami K., Rezzolla L., Yoshida S., 2011, *MNRAS*, **416**, L1

Uryū K., Tsokaros A., Baiotti L., Galeazzi F., Taniguchi K., Yoshida S., 2017, *Phys. Rev. D*, **96**, 103011

Uryū K., Tsokaros A., Galeazzi F., Hotta H., Sugimura M., Taniguchi K., Yoshida S., 2016, *Phys. Rev. D*, **93**, 044056

Watts A. L., Andersson N., Jones D. I., 2005, *ApJ*, **618**, L37

Weih L. R., Most E. R., Rezzolla L., 2018, *MNRAS*, **473**, L126

Wilson J. R., Mathews G. J., Marronetti P., 1996, *Phys. Rev. D*, **54**, 1317

Xie X., Hawke I., Passamonti A., Andersson N., 2020, *Phys. Rev. D*, **102**, 044040

Zhou E., Tsokaros A., Uryū K., Xu R., Shibata M., 2019, *Phys. Rev. D*, **100**, 043015

APPENDIX A: RESCALED EQUATIONS FOR CODE IMPLEMENTATION

As in all KEH-type codes, so in the rns code, key equations and quantities are rescaled with the coordinate equatorial radius r_e for the computations. In this appendix we summarise the relevant rescaled expressions used in this work.

The rescalings for the angular velocity Ω , the gravitationally redshifted angular momentum per unit rest mass F , the metric potentials ρ , γ , ω and the parameters A and B , are given by the following expressions

$$\begin{aligned}\hat{\Omega} &= r_e \Omega, & \hat{F} &= F/r_e, & \hat{\rho} &= \rho/r_e^2, & \hat{\gamma} &= \gamma/r_e^2, \\ \hat{\omega} &= r_e \omega, & \hat{A} &= A/r_e, & \hat{B} &= B/r_e.\end{aligned}\quad (\text{A1})$$

We note that the rescaling for F emerges if we take equation (27) and apply the rescaling relations for Ω , ω and ρ

$$F = u^t u_\phi = \frac{r_e (\hat{\Omega} - \hat{\omega}) s^2 (1 - \mu^2) e^{-2r_e^2 \hat{\rho}}}{(1 - s)^2 - (\hat{\Omega} - \hat{\omega})^2 s^2 (1 - \mu^2) e^{-2r_e^2 \hat{\rho}}} = r_e \hat{F}, \quad (\text{A2})$$

where $\mu = \cos \theta$ and $s = r/(r + r_e)$ is the compactified radial coordinate mapping radial infinity to the finite coordinate location $s = 1$ (Cook et al. 1992). Concerning the rescalings of parameters A and B , we expect the fractions $\frac{F}{A^2 \Omega_c}$ and $\frac{F}{B^2 \Omega_c}$ from the differential rotation law (14) to be dimensionless. This demand, together with applying the rescalings for F and Ω , leads to the specific rescalings of parameters A and B reported in (A1).

A stepping stone towards obtaining final expressions for a new Ω_e value and for calculating Ω everywhere inside the star, is to obtain rescaled relations for F_e and F_{\max} , as well as parameters A and B in the general case, i.e. equations (23), (24). Therefore, we apply (A2) at the equator (where $\mu = 0$ and $s = 0.5$) to obtain

$$F_e = \frac{r_e v_e^2}{(1 - v_e^2) (\hat{\Omega}_e - \hat{\omega}_e)} = \frac{r_e (\hat{\Omega}_e - \hat{\omega}_e) e^{-2r_e^2 \hat{\rho}_e}}{\left[1 - (\hat{\Omega}_e - \hat{\omega}_e)^2 e^{-2r_e^2 \hat{\rho}_e}\right]} = r_e \hat{F}_e, \quad (\text{A3})$$

and at the location of the maximum of Ω (again at the equatorial plane $\mu = 0$) to obtain

$$\begin{aligned}F_{\max} &= \frac{r_e v_{\max}^2}{(1 - v_{\max}^2) (\hat{\Omega}_{\max} - \hat{\omega}_{\max})} \\ &= \frac{r_e (\hat{\Omega}_{\max} - \hat{\omega}_{\max}) s_{\max}^2 e^{-2r_e^2 \hat{\rho}_{\max}}}{\left[(1 - s_{\max})^2 - (\hat{\Omega}_{\max} - \hat{\omega}_{\max})^2 s_{\max}^2 e^{-2r_e^2 \hat{\rho}_{\max}}\right]} \\ &= r_e \hat{F}_{\max}.\end{aligned}\quad (\text{A4})$$

Moving on to apply the rescalings (A1) to equations (23) and (24), the general analytic expressions to calculate the parameters A and B are written as

$$\hat{A}^2 = \frac{1}{\hat{\Omega}_c} \left[(\hat{F}_e \hat{F}_{\max})^p \frac{(\lambda_2 \hat{F}_e^q - \lambda_1 \hat{F}_{\max}^q)}{[(\lambda_1 - 1) \hat{F}_e^p - (\lambda_2 - 1) \hat{F}_{\max}^p]} \right]^{\frac{1}{p+q}}, \quad (\text{A5})$$

$$\hat{B}^2 = \frac{\hat{F}_e \hat{F}_{\max}}{\hat{\Omega}_c} \left[\frac{(\lambda_2 \hat{F}_e^q - \lambda_1 \hat{F}_{\max}^q)}{[\lambda_2 (\lambda_1 - 1) \hat{F}_e^{p+q} - \lambda_1 (\lambda_2 - 1) \hat{F}_{\max}^{p+q}]} \right]^{1/p}. \quad (\text{A6})$$

We note that, compared to the initial equations, there are no differences in r_e terms introduced, i.e. after all rescaled quantities are substituted in both the right and left hand sides, occurrences of r_e eliminate each other.

Next, we turn to the main equations for calculating a new value

for Ω_e and Ω everywhere inside the star. Substituting the rescalings (A1) into equations (26) and (30) we obtain, respectively

$$\begin{aligned}r_e^2 (\hat{\gamma}_e + \hat{\rho}_e - \hat{\gamma}_p - \hat{\rho}_p) + \ln \left[1 - (\hat{\Omega}_e - \hat{\omega}_e)^2 e^{-2r_e^2 \hat{\rho}_e} \right] = \\ - 2 \hat{\Omega}_e \frac{(\hat{\Omega}_e - \hat{\omega}_e) e^{-2r_e^2 \hat{\rho}_e}}{\left[1 - (\hat{\Omega}_e - \hat{\omega}_e)^2 e^{-2r_e^2 \hat{\rho}_e} \right]} \\ + \frac{\hat{A}^2 \hat{\Omega}_e^2}{2 \lambda_2^2} \left\{ 2 \frac{\hat{A}^2}{\hat{B}^2} \arctan \left(\frac{\lambda_2^2 (\hat{\Omega}_e - \hat{\omega}_e)^2 e^{-4r_e^2 \hat{\rho}_e}}{\hat{A}^4 \hat{\Omega}_e^2 \left[1 - (\hat{\Omega}_e - \hat{\omega}_e)^2 e^{-2r_e^2 \hat{\rho}_e} \right]^2} \right) \right. \\ - \sqrt{2} \left[\arctan \left(1 - \frac{\lambda_2 \sqrt{2} (\hat{\Omega}_e - \hat{\omega}_e) e^{-2r_e^2 \hat{\rho}_e}}{\hat{A}^2 \hat{\Omega}_e \left[1 - (\hat{\Omega}_e - \hat{\omega}_e)^2 e^{-2r_e^2 \hat{\rho}_e} \right]} \right) \right. \\ \left. \left. - \arctan \left(1 + \frac{\lambda_2 \sqrt{2} (\hat{\Omega}_e - \hat{\omega}_e) e^{-2r_e^2 \hat{\rho}_e}}{\hat{A}^2 \hat{\Omega}_e \left[1 - (\hat{\Omega}_e - \hat{\omega}_e)^2 e^{-2r_e^2 \hat{\rho}_e} \right]} \right) \right] \right\} \\ + \sqrt{2} \tanh^{-1} \left(\frac{\frac{\hat{A}^2 \hat{\Omega}_e \sqrt{2}}{\lambda_2} \frac{(\hat{\Omega}_e - \hat{\omega}_e) e^{-2r_e^2 \hat{\rho}_e}}{\left[1 - (\hat{\Omega}_e - \hat{\omega}_e)^2 e^{-2r_e^2 \hat{\rho}_e} \right]}}{\frac{(\hat{\Omega}_e - \hat{\omega}_e)^2 e^{-4r_e^2 \hat{\rho}_e}}{\left[1 - (\hat{\Omega}_e - \hat{\omega}_e)^2 e^{-2r_e^2 \hat{\rho}_e} \right]^2} + \frac{\hat{A}^4 \hat{\Omega}_e^2}{\lambda_2^2}} \right) \Bigg\}, \quad (\text{A7})\end{aligned}$$

for the relation to find a new value for Ω_e , and

$$\begin{aligned}\hat{\Omega} = \hat{\Omega}_c \frac{1 + \left(\frac{(\hat{\Omega} - \hat{\omega}) s^2 (1 - \mu^2) e^{-2r_e^2 \hat{\rho}}}{\hat{B}^2 \hat{\Omega}_c \left[(1 - s)^2 - (\hat{\Omega} - \hat{\omega})^2 s^2 (1 - \mu^2) e^{-2r_e^2 \hat{\rho}} \right]} \right)^p}{1 + \left[\frac{(\hat{\Omega} - \hat{\omega}) s^2 (1 - \mu^2) e^{-2r_e^2 \hat{\rho}}}{\hat{A}^2 \hat{\Omega}_c \left[(1 - s)^2 - (\hat{\Omega} - \hat{\omega})^2 s^2 (1 - \mu^2) e^{-2r_e^2 \hat{\rho}} \right]} \right]^{p+q}}.\end{aligned}\quad (\text{A8})$$

for the relation to calculate a new distribution for Ω everywhere inside the star.

Finally, applying the rescalings (A1) to the new equation derived for the calculation of the enthalpy (31) and taking into account expression (32) for the integral term, we obtain the following relation for the enthalpy

$$\begin{aligned}H = H_{\text{surface}} + \frac{1}{2} \left[r_e^2 (\hat{\gamma}_p + \hat{\rho}_p - \hat{\gamma} - \hat{\rho}) - \ln (1 - v^2) \right] \\ - \hat{F} \hat{\Omega} + \frac{\hat{A}^2 \hat{\Omega}_c^2}{4} \left\{ \frac{2 \hat{A}^2}{\hat{B}^2} \arctan \left(\frac{\hat{F}^2}{\hat{A}^4 \hat{\Omega}_c^2} \right) \right. \\ - \sqrt{2} \left[\arctan \left(1 - \frac{\hat{F} \sqrt{2}}{\hat{A}^2 \hat{\Omega}_c} \right) - \arctan \left(1 + \frac{\hat{F} \sqrt{2}}{\hat{A}^2 \hat{\Omega}_c} \right) \right] \\ \left. + \sqrt{2} \tanh^{-1} \left(\frac{\hat{A}^2 \hat{\Omega}_c \hat{F} \sqrt{2}}{\hat{F}^2 + \hat{A}^4 \hat{\Omega}_c^2} \right) \right\}.\end{aligned}\quad (\text{A9})$$

We stress that (A7) and (A9) are derived for the particular case of $\{p, q\} = \{1, 3\}$.

APPENDIX B: COMPARISON BETWEEN GR AND IWM-CFC MODELS

Building on our previous work (Iosif & Stergioulas 2014), we present here a comparison between GR and the spatially, conformally flat, spacetime approximation IWM-CFC (Isenberg 2008; Wilson et al. 1996) for the case of equilibrium models with $r_p/r_e \sim 0.5$, constructed with the Uryu+ differential rotation law (14).

In the context of the IWM-CFC approximation, the basic assumption is conformal flatness for the spatial metric

$$\gamma_{ij} = \psi^4 \eta_{ij}, \quad (\text{B1})$$

where ψ is a conformal factor and η_{ij} is the flat metric. Writing the line element in the 3 + 1 formalism of general relativity we have

$$ds^2 = -\alpha^2 dt^2 + \gamma_{ij}(dx^i + \beta^i dt)(dx^j + \beta^j dt), \quad (\text{B2})$$

where α is the lapse function and β^i is the shift vector. If we now consider an axisymmetric star, in spherical-like coordinates and in the absence of meridional circulation, β^ϕ is the only non-zero component of the shift vector β^i . Therefore, combining equations (B1) and (B2), the line element is expressed as

$$ds^2 = -\alpha^2 dt^2 + \psi^4(dr^2 + r^2 d\theta^2) + \psi^4 r^2 \sin^2 \theta (d\phi + \beta^\phi dt)^2. \quad (\text{B3})$$

Going back to the line element (1) for a stationary, axisymmetric star in full GR and comparing with (B3) above, implies that

$$\alpha = e^{(\gamma+\rho)/2}, \quad \psi = e^{\mu/2} = e^{(\gamma-\rho)/4}, \quad \beta^\phi = -\omega. \quad (\text{B4})$$

This means that the line element (1) can take the IWM-CFC form, if

$$\mu = \frac{\gamma - \rho}{2}. \quad (\text{B5})$$

In summary, a numerical code (such as `rns`) that solves for the full GR metric (1) can be easily converted to also handle the case of the IWM-CFC approximation, by imposing the condition (B5) between the three metric functions instead of solving for the metric potential μ .

Following the above reasoning, we constructed IWM-CFC counterparts for models A9, B10, C5 that exhibit $r_p/r_e \sim 0.5$ assuming the new 4-parameter Uryu+ rotation law (14) and we compared them to their respective full GR configurations. Our findings are summarised in Table B1. For the lowest density configuration A9, the relative error between GR and CFC is at most $\sim 0.2\%$ (for the angular velocity of a free particle in circular orbit at the equator Ω_K) and lower for integrated quantities. Moving on to the denser model B10, the relative error is at the 1% level for local quantities, such as the angular velocities and the radii, whereas it remains below 1% for the masses M , M_0 and the ratio $T/|W|$. This general picture does not change much for the more compact model C5, where the relative error for local quantities rises to $\sim 2.5\%$ and remains $\sim 1\%$ for the masses and the ratio $T/|W|$. We should point out that the largest relative error between GR and CFC is encountered for the angular momentum J but even that is only $\sim 2.7\%$.

As a further check, in Figure B1 we present the energy density and angular velocity profiles, $\epsilon(r)$ and $\Omega(r)$, for model C5 constructed with the Uryu+ rotation law (14) both in full GR and in the IWM-CFC approximation. The results underline the robustness of the IWM-CFC method as a viable approximation in numerical simulations of BNS merger remnants, when an accuracy of order $\sim 1\%$ is sufficient.

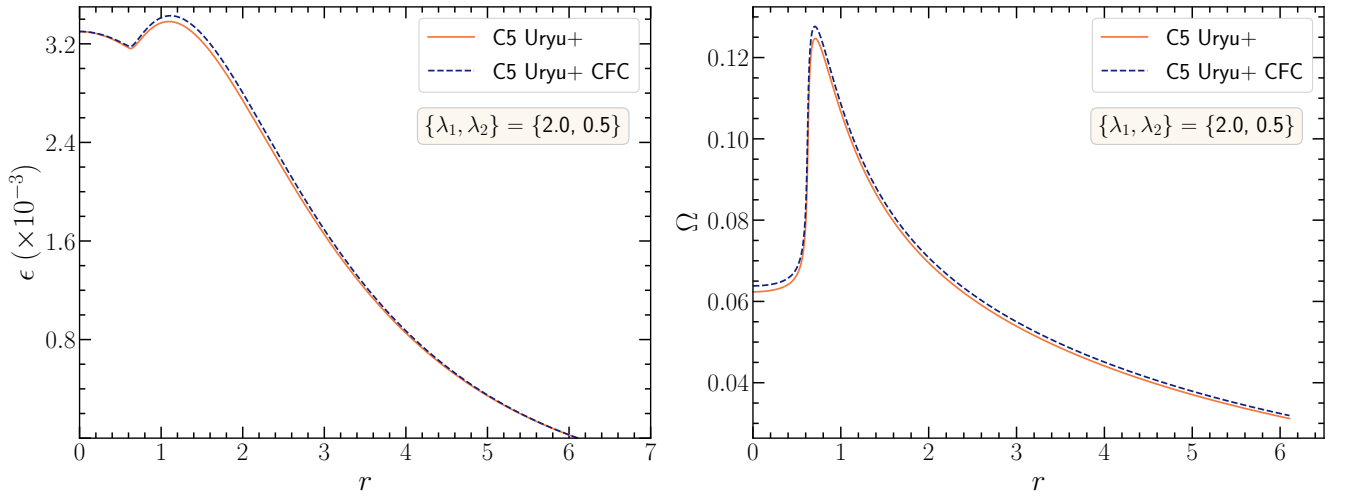
APPENDIX C: ADDITIONAL SEQUENCE C MODEL WITH THE KEH ROTATION LAW

In Figures 5 and 7 we used an additional model along sequence C, constructed with the KEH rotation law that was not part of the original sequence C in Iosif & Stergioulas (2014). In Table C1 we list the detailed properties of this model.

This paper has been typeset from a \LaTeX file prepared by the author.

Table B1. Comparison of the properties of equilibrium models constructed with the Uryu+ rotation law, in full GR and in the IWM-CFC approximation, for models A9, B10, C5 (which have $r_p/r_e \sim 0.5$).

Model	ϵ_{\max} ($\times 10^{-3}$)	M	M_0	J	$T/ W $ ($\times 10^{-1}$)	Ω_c ($\times 10^{-2}$)	Ω_{\max} ($\times 10^{-2}$)	Ω_e ($\times 10^{-2}$)	Ω_K ($\times 10^{-2}$)	R_e	r_e	GRV3
A9												
GR	0.40086	1.43493	1.50612	1.96591	1.64514	1.97549	3.95098	0.98775	2.28329	14.5499	12.9843	6.03066e-05
CFC	0.40140	1.43389	1.50509	1.96210	1.64425	1.97906	3.95812	0.98953	2.28836	14.5253	12.9608	1.30367e-02
rel. error (%)	0.13321	0.07248	0.06839	0.19380	0.05410	0.18071	0.18071	0.18051	0.22205	0.16907	0.18099	
B10												
GR	1.48092	2.20535	2.41490	3.63795	1.65695	4.10748	8.21495	2.05374	4.15491	10.9145	8.42730	5.64007e-05
CFC	1.49134	2.19289	2.40250	3.59161	1.65022	4.15271	8.30543	2.07636	4.20732	10.8046	8.33003	2.81039e-02
rel. error (%)	0.70362	0.56499	0.51348	1.27379	0.40617	1.10116	1.10141	1.10141	1.26140	1.00692	1.15422	
C5												
GR	3.38103	2.16935	2.37578	3.36450	1.64806	6.23604	12.4721	3.11802	5.73080	8.60458	6.10795	5.50829e-05
CFC	3.42815	2.14125	2.34785	3.27299	1.63242	6.38268	12.7654	3.19134	5.87823	8.42468	5.95685	3.42459e-02
rel. error (%)	1.39366	1.29532	1.17561	2.71987	0.94899	2.35149	2.35165	2.35149	2.57259	2.09075	2.47383	

**Figure B1.** Comparison of the energy density and angular velocity profiles, $\epsilon(r)$ and $\Omega(r)$, versus the coordinate radius r , in the equatorial plane for model C5 ($r_p/r_e = 0.5$), calculated in full GR and in the IWM-CFC approximation, for the Uryu+ rotation law.**Table C1.** Physical quantities of an additional model along sequence C (with constant $\epsilon_c = 3.3 \times 10^{-3}$), constructed with the KEH rotation law ($\hat{A} = 1$).

r_p/r_e	ϵ_c ($\times 10^{-3}$)	ϵ_{\max} ($\times 10^{-3}$)	M	M_0	J	$T/ W $ ($\times 10^{-1}$)	Ω_c ($\times 10^{-2}$)	Ω_e ($\times 10^{-2}$)	Ω_K ($\times 10^{-2}$)	R_e	r_e	GRV3 ($\times 10^{-5}$)
0.43	3.300	3.66772	2.26784	2.48488	3.96229	1.85476	14.6252	3.55694	5.64641	8.81100	6.16946	4.89800